Modeling and Analysis of Core-Shell Si/SiGe Nanowires

by

Ming Y. Tang

B.S. in Electrical Engineering Computer Science
& Materials Science and Engineering
University of California, Berkeley (2001)

Submitted to the Department of Electrical Engineering and Computer Science
in partial fulfillment of the requirements for the degree of

Master of Science in Electrical Engineering and Computer Science

at the

MASSACHUSETTS INSTITUTE OF TECHNOLOGY

August 2004

Author . . . .
Department of Electrical Engineering and Computer Science
August 18, 2004

Certified by . . . .
Mildred S. Dresselhaus
Institute Professor of Electrical Engineering and Physics
Thesis Supervisor

Accepted by . . . .
Arthur C. Smith
Chairman, Department Committee on Graduate Students

Modeling and Analysis of Core-Shell Si/SiGe Nanowires

by

Ming Y. Tang

Submitted to the Department of Electrical Engineering and Computer Science
on August 18, 2004, in partial fulfillment of the
requirements for the degree of
Master of Science in Electrical Engineering and Computer Science

Abstract

In this thesis, I present a theoretical model for the Si core/SiGe shell core-shell nanowire system. A model for the single carrier pocket core-shell nanowire is first developed, along with the boundary conditions of a circular wire and sharp interfaces between the two media. A numerical scheme is then developed for the core-shell nanowire system, along with educated approximations for the numerical boundary conditions. The numerical model is designed such that low energy levels have higher accuracy than the high energy levels.

The core-shell nanowire model is applied to a Si core/SiGe alloy shell structure, which is considered as a core-shell nanowire building block containing multiple carrier pockets. Based on the 2D band structure of strained SiGe on a Si substrate, the strained SiGe layer of the Si core/SiGe shell core-shell nanowire is modeled. The effect of different parameters (the interface offset energy V, the total core-shell diameter e, and the core diameter d) on the energy levels of the Si/SiGe core-shell nanowire system is investigated. It is found that the core-shell nanowire system with the greatest quantum mechanical effect is the one with a small e, a relatively small magnitude V, and a d that results in a secondary confinement effect in the lower potential energy region.

A 1D semi-classical transport model for the core-shell nanowire structure based on the Boltzmann transport equation is developed. Applying the 1D semi-classical model to the Si core/SiGe shell core-shell nanowire system, the thermoelectric properties of this particular system and the effect of doping on these properties are investigated. It is found that the system with an optimal doping concentration (n_{opt} or p_{opt}), a small V, a small e, a small d, and a shell with a composition that results in a high mobility has a very promising thermoelectric performance.

Lastly, the thermoelectric-related transport properties for a Si/SiGe core-shell nanowire are compared with the related properties for a Si nanowire and a SiGe nanowire. The Si/SiGe core-shell nanowire shows a better thermoelectric performance than its Si nanowire counterpart. On the other hand, by relaxing the harsh conditions imposed on the carrier mobility of the Si/SiGe core-shell nanowire structure in this thesis, the Si/SiGe core-shell nanowire structure is also expected to have a better thermoelectric performance than its SiGe nanowire counterpart.

Thesis Supervisor: Mildred S. Dresselhaus
Title: Institute Professor of Electrical Engineering and Physics

Acknowledgments

I have never imagined going this far in education. Today's success in education would have never come true without the support, love, nurture, and caring from my teachers, my mentors, my friends, my relatives, my advisor Professor Millie Dresselhaus, my grandparents, my girlfriend Elizabeth Liu, my brother Eric Tang, my father Tang Sun Shing, and most importantly, my mother Chan Yin Ngan.

My long education journey started all the way back in Hong Kong at the Salvation Army Tin Ka Ping Primary School. I like to thank all of the teachers that had taught me during the period from Fall 1985 to Spring 1991. I especially like to thank Mr. Cheng for inspiring me on the subject of mathematics and for helping me to master the game of "Health Happy Chess".

Coming to US is an enormous adjustment for me, especially my first few years. I would have never been the same without the supports and mentoring from my teachers in Cedarlane Middle School and Glen A. Wilson High School. I thank all of the teachers and peers that had given me valuable advice and counseling.

My undergraduate in UC Berkeley is another extremely rewarding experience. Without the encouragements and guidance from many of my professors, my supervisors, and my friends, I would not have made it to graduate school. I like to especially thank Professor Ronald Gronsky, Professor Andreas Glaeser, Professor Timothy Sands, Professor Michael Crommie, Mr. Mike Leong, and Ms. Jane Stanley for their valuable mentoring and support during my graduate school application period.

My two years at MIT are both exciting and rewarding experience. I have learned tremendous amount of knowledge from both my colleagues and my professors.

I like to first thank Professor Tayo Akinwande by giving me the opportunity to TA 6.012 (Microelectronic Devices and Circuits) during my first semester at MIT. I also like to thank Professor Clifton Fonstad and Professor Donald Troxel for their support during my TA experience. I especially like to thank my fellow co-TA Dr. Akin Aina for his constant support and mentoring, both at and away from work.

Besides my rewarding TA experience, I also had an exciting and fun class experience. I like to thank Micah O'Halloran being the best and coolest TA of my life. His help and support in 6.376 (Low Power Analog VLSI) really helped ease me in during my first semester at MIT. The laugher and jokes in the computer lab from my intelligent classmates Rayal Johnson and Belal Helal, my brilliant project partner Dr. Syed Alam, and my extremely smart and beautiful classmate Ghinwa Choueiter had really made my 6.376 project experience both fun and unforgettable. I especially like to thank Ghinwa Choueiter for her constant supply of tasty cookies to keep me from starving during all those late night project times.

Finding the right research group was never an easy task. During my group searching period, I like to thank Professor Michael Perrott and Professor Terry Orlando for their mentoring and suggestions. I especially like to thank Song-Hee Paik for her supports and encouragements during this difficult period. Without them, I probably would not have stayed at MIT. I thanked them with all my heart.

I was very grateful that I joined Professor Millie Dresselhaus' mgm research group. I like to thank the warm welcome from Professor Millie Dresselhaus, Dr. Gene Dresselhaus, Laura Doughty, Dr. Yu-Ming Lin, Dr. Marcie Black, Dr. Adelina Santos, Dr. Oded Rabin, Grace Chou, Georgii Samsonidze, Hyungbin Son, Nasser Demir, Bosun Adeoti, and Victor Brar.

During this short a year and a half period in the mgm group, I not only learned how to do research, I also learned many useful technical and nontechnical skills. Millie's work enthusiasm, love of science, and work ethics have truly inspired and amazed me. She is one special human being. I sincerely like to thank Millie for giving me this research opportunity and for being extremely patient throughout my learning period.

This group is never the same without the presence of Dr. Gene Dresselhaus. Gene is a true Cal Bear. GO BEARS!!! I thank him for all his research suggestions, Latex support, and his humor. I truly respect his continuous resistant spirit against Microsoft products.

I like to thank Laura Doughty for her constant support and advice. Laura is a great singer and I really enjoy both her concert and her singing in the hallway.

I also like to thank Dr. Yu-Ming Lin, Dr. Marcie Black, and Dr. Oded Rabin for their mentoring in quantum mechanics, solid state physics, and thermoelectrics. Without their patience in teaching, I would have never had the proper background to produce this thesis. I especially like to thank Dr. Yu-Ming Lin and Dr. Oded Rabin for teaching me the different ways of making single crystal and polycrystal Bi nanowires. I also like to thank them for their continuous support and mentoring even after their graduation. It was a memorable time to share an office with Dr. Oded Rabin. I enjoy the jokes and the science we talked about in the office.

It was also a joyful time to interact with other non-thermoelectrics mgm group members. I like to thank Grace Chou for giving me the valuable lesson on the operation of Raman spectroscopy and on perturbation theory. Grace is definitely a fun person and she brings a lot of happiness into this group. I hold a great appreciation for Georgii Samsonidze's computer networking support and computer software support. Without Georgii Samsonidze, the computers in this group will never be the same. I also like to thank Hyungbin Son, Nasser Demir, Bosun Adeoti, Victor Brar, Eduardo Barros, Daniel Nezich, and Professor Riichiro Saito for their special characters that shine on me.

This thesis would not be possible without our thermoelectrics collaborators from MIT and Boston College. I like to thank Professor Gang Chen and Professor Zhifeng Ren for their continuous support and mentoring. I especially like to thank Chris Dames for his brilliant suggestions and ideas. I also like to thank Hohyun Lee and Dr. Dezhi Wang for their measurement side of support and fabrication side of support of our joint project, respectively.

Besides conducting research during my time in mgm, I also took different classes to enrich my background. With my most sincere appreciation, I like to thank Professor Rajeev Ram for his patience in explaining the subject of solid state physics. I also like to thank Professor Peter Hagelstein for his exciting lectures in both 6.728 (Applied Quantum and Statistical Physics) and 6.673 (Introduction to Numerical Simulation in Electrical Engineering), and his understanding in students' schedule conflict. I enjoyed his graduate school stories very much. I also like to thank Irfan Chaudhary for being extremely helpful and responsible in 6.728.

Teamwork is definitely the key to success in this world. I like to thank Melinda Wong for being a good homework partner for both 6.728 and 6.730 (Physics for Solid-State Applications). I like to thank Professor Terry Orlando once again for being a fabulous teacher in 6.730.

Besides school, I also get to know many good friends outside of classes and research. I first like to thank Debb Hodges-Pabon for organizing the EECS open house in March 2002 to give me an opportunity to know more about MIT and to mingle with many incoming EECS graduate students. I like to thank all of my fellow Tang crews for constantly giving me the love, the care, the support, and the fun ever since I stepped footage on MIT. I especially like to thank Tony Lau's stress-relieved brain-freezer smoothie, Shawn Kuo's Walmart cereal stock up trips, Tyrone Hill's weightlifting company, Steve Kohen's tasty desserts and cakes, Chris Rycroft's English pancake and home-made dinner, Katherine Ryan's banana chocolate chip bread, Vivian Lei's constant funny laughes and amusing behaviors, Natalija Jovanovic's mom-like caring comments, Karen Lee's unpredictable sarcasm, and Johnna Powell's lunch company.

I also like to thank my fellow friends in the HKSBS (Hong Kong Student Bible Study Group at MIT) for their prayers and care. I especially like to thank Sam Au, Ernie Yeh, and Becky Poon for always being like a big brother or a big sister to me and always giving me guidance and support.

I am very fortunate that not only was I surrounded by my friends and my family, but also by my love one. To my dearest girlfriend Elizabeth Liu, I owe my deepest appreciation for your love and caring during this period. My graduate school life would have never been the same without your presence in my life.

Lastly, none of this would be realized without the unconditioned love and care from my brother Eric Tang, my father Tang Sun Shing, and most importantly, my mother Chan Yin Ngan. I thank them for always being there for me. I like to thank my parents for all these 25 years of unconditional nurture and continuous advice. I especially like to thank my mother for always being there for me ever since my birth, both physically and mentally.

I like to dedicate this thesis to my grandfather and grandmother who are no long with us. I thank them for always taking care of my brother and me during our childhood during the weekday nights and over the weekends while my parents were at work. I also like to thank them for throwing incredible birthday parties for my brother and me. I especially thank them for all these years of unreserved love, care, and tremendous amount of encouragement.

Contents

List of Figures

List of Tables

Chapter 1

Introduction

This thesis starts off with some background information on the topic of thermoelectrics. It is then followed by the motivation for this thesis work and the outline of this thesis.

1.1 Background

Thermoelectrics can be dated all the way back to 19th century. In 1821, Thomas Seebeck discovered that an electromotive force could be produced by heating a junction between two metals. Following Seebeck's discovery, in 1834, Jean Peltier discovered that passing an electric current through the junction between two dissimilar conductors could result in a cooling effect. More importantly, in 1855, William Thomson (later Lord Kelvin) not only predicted a third thermoelectric effect, he also derived the relationship between thermoelectric effects using thermodynamic arguments. Resulting from these discoveries, the idea of thermoelectric materials was born. However, it was not until the invention of the transistor in 1949 that researchers started seriously looking into thermoelectric applications [6].

Since the birth of transistor, interest in the field of thermoelectric materials skyrocketed. The field of thermoelectrics was especially active during the 1957-1965 period. Much improvement in thermoelectric materials was made during this period, especially after the proposal in 1956 by Abram Ioffe and his co-workers that doped semiconducting materials were the best candidates for thermoelectric materials and that alloying could reduce the lattice thermal conductivity in a major way without much deterioration to the other thermoelectric parameters [6]. Unfortunately, following this very active period, little improvement was achieved, and the search of good thermoelectrics materials became rather inactive for the next thirty year period.

Since the birth of thermoelectric materials, the two major thermoelectric applications have been for refrigeration and for the generation of electricity from heat. The advantage of thermoelectric refrigeration is the absence of moving compressor units as is done in the conventional way of refrigeration. Thermoelectrics not only decreases the noise level and the weight of the refrigerator, it also increases the refrigerator life cycle. Furthermore, thermoelectric electricity generation is commonly used in space applications. The most common application is to generate electricity using the temperature difference between the inside and outside of the spacecraft. The thermal energy for space applications is supplied by a radioactive source and by sunlight. This is a very important and essential application, since only a limited amount of fuel is available in a spacecraft and solar energy becomes too weak for use in deep space missions, where thermoelectricity is the only viable technology presently available for supplying energy aboard the spacecraft.

With increasing pressures for space explorations, increasing demands for using lighter materials for space applications, and increasing demands of the US Navy to have quiet submarines, researchers have once again turned to the topic of thermoelectricity. In the 1990s, using low dimensional physics concepts, Hicks and Dresselhaus predicted that a dramatic enhancement in thermoelectric performance was possible through the use of quantum wells and quantum wires [7, 8]. At the same time, nanofabrication technology rapidly improved during the last decade. With the advance in technology and new low dimensional ideas, improvements in thermoelectric efficiency

($ZT = S^2\sigma T/(\kappa_e + \kappa_L)$ where σ is the electrical conductivity, S is the Seebeck coefficient, κ_e is the electrical thermal conductivity, κ_L is the lattice thermal conductivity, and T is the temperature) have been demonstrated. For example, room temperature (T=25°C) values of the dimensionless thermoelectric figure of merit $ZT \sim 2.4$ have recently been achieved for a p-type Bi_2Te_3/Sb_2Te_3 superlattice device [9]. These promising trends have once again ignited the interest of the research community in the area of thermoelectrics.

1.2 Motivation

Although low dimensional systems gave much hope for improving thermoelectric materials, it comes at a rather high cost. Making low dimensional systems is a very time-consuming and expensive process. The equipments involved usually are very expensive as well. The result is that low dimensional thermoelectrics today are not competitive on a cost basics with other thermoelectric materials. Thus we are motivated to find a way to implement the development of a cost-effective low dimensional system.

The proposed cost-effective low dimensional system is a self-assembled composite nanostructured materials system (see Figure 1-1). The nanostructured materials consist of either nanowires or nanoparticles. Thus, the building block of the composite system is either core-shell nanowires or core-shell nanoparticles.

In this thesis, the materials under consideration are Si, Ge, and SiGe alloys. Bulk SiGe alloys already have been shown to have rather good thermoelectric properties at high temperature for space applications. The goal of this work is to introduce nanowires or nanoparticles inside the SiGe alloys host material to improve its thermoelectric performance. This thesis focuses on Si nanowires as the low-dimensional building block material, while SiGe alloys are the host material. Thus, the building block of the composite will be a Si core and a SiGe alloy shell in a core-shell nanowire

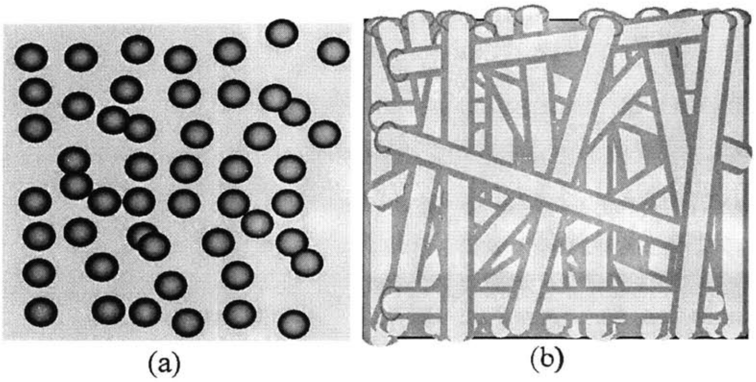

Figure 1-1: (a) Si nanoparticles embedded in a Ge host material composite structure, and (b) Si nanowires embedded in a Ge host material composite structure.

building block structure.

A detailed analysis is performed on this thermoelectric building block nanostructure at room temperature. With the extra interface introduced by the Si core/SiGe shell structure, the thermal conductivity of each of the building blocks is expected to decrease, resulting in an expected enhanced thermoelectric performance. The thermoelectric performance improvement of the building blocks in turn is expected to give an overall improvement in performance for the composite structure.

1.3 Thesis Outline

In Chapter 2, the basic modeling of a core-shell nanowire is presented. Assumptions and approximations for the boundary conditions are given. The Schrödinger equation for the core-shell nanowire is derived. A numerical scheme based on a three point center differencing method is used to solve the Schrödinger equation numerically for a single carrier pocket in the core and a single carrier pocket in the shell. The chapter ends with a comparison with previous nanowire numerical solutions.

Chapter 3 applies the model derived in Chapter 2 to the Si core/SiGe alloys shell in core-shell nanowire building blocks containing multiple carrier pockets. A brief review of the properties of Si, Ge and SiGe alloys constituents, along with consideration of the strain effect on the SiGe alloys band structure are presented. Assumptions and approximations are made for the Si/SiGe core-shell nanowire building blocks. The chapter concludes with the effect of different parameters (interface offset V, total core-shell diameter e, and core diameter d) on the energies of the core-shell nanowire building block system.

Chapter 4 focuses on the thermoelectric-related transport properties of the Si/SiGe building block. A 1D semi-classical transport model for the core-shell nanowire based on the Boltzmann transport equation is developed along with the assumptions and approximations that are used to solve the Boltzmann equation. The detailed investigation of doped Si/SiGe core-shell nanowires is then presented. The chapter ends with the effect of different parameters (doping concentration, e, and d) on ZT.

Lastly, this thesis closes with Chapter 5 on conclusions and future research directions.

Chapter 2

Modeling of the Core-Shell Nanowire

This chapter sets up the Schrödinger equation for the core-shell nanowire system. The framework of this formulation follows closely from the previous calculation of the nanowire system [10]. The Schrödinger equation for the core-shell nanowire system is then solved numerically and checked against the previous nanowire numerical solution [10].

2.1 Assumptions and Approximations of the Boundary Conditions

Figure 2-1 shows a schematic of a single core-shell nanowire. There are two interfaces in a single core-shell nanowire: the interface between the core material and the shell material, and the interface between the shell material and the environment. In this thesis, the interface will be modeled as a sharp potential offset. The environment outside the core-shell nanowire will be modeled as an infinite potential. Thus, this core-shell nanowire system is similar to a 1D potential well surrounded by an infinite barrier, with the exception that there is an additional potential offset in the middle

Figure 2-1: A core-shell nanowire structure. d and e denote the core diameter and the total core-shell diameter, respectively.

core region.

2.2 Schrödinger Equation for the Core-Shell Nanowire

In a period crystal, the electron wavefunction is composed of a periodic function (Bloch function) and an envelope function. From the effective mass theorem [11], knowing the envelope wave function is sufficient to describe many properties of the system. Therefore, it is sufficient within the effective mass approximation to solve for the envelope function of the system without solving for the exact wavefunction.

Consider an infinitely long core-shell circular wire with an inner material A with core diameter of d and an outer material B with thickness of $(e-d)/2$, resulting in a total core-shell diameter of e. Consider a single carrier pocket in both the core and the shell of the core-shell nanowire system as an example. When detailed calculations are done in Chapters 3 and 4, the appropriate carrier pockets are all included for both the core and shell regions. In general, not only is the wire axis oriented along an arbitrary direction with respect to the crystallographic directions of the materials, but the two materials themselves also will have different crystallographic directions. Thus, a total of 3 different set of axes are needed to specify the core-shell nanowire system: the wire, the core material, and the shell material. We define the z axis as the wire axis and the x and y axes as the axes that lie in the cross-sectional plane of the wire. We also define the xj axis, the yj axis, and the zj axis to be the three principal axes of the carrier pocket of material j. The effective mass tensor of an anisotropic carrier pocket of a cubic material j in its crystallographic coordinate system (xj, yj, zj) is given by

$$M_{crystal,j} = \begin{pmatrix} m_{x,j} & 0 & 0 \\ 0 & m_{y,j} & 0 \\ 0 & 0 & m_{z,j} \end{pmatrix}. \tag{2.1}$$

With a proper coordinate transformation ($M_{wire,j} = R_{crystal->wire} \cdot M_{crystal,j} \cdot R^{-1}_{crystal->wire}$ where $R_{crystal->wire}$ is the transformation matrix that transforms the crystal coordinates to the wire coordinates), the effective mass tensor of an anisotropic carrier pocket of material j in the wire coordinates (x, y, z) can be obtained to be

$$M_{wire,j} = \begin{pmatrix} m_{11,j} & m_{12,j} & m_{13,j} \\ m_{12,j} & m_{22,j} & m_{23,j} \\ m_{13,j} & m_{23,j} & m_{33,j} \end{pmatrix}. \tag{2.2}$$

One should note that the mass tensor $M_{wire,j}$ is a symmetrical tensor. With the mass tensor in Equation (2.2), the dispersion relation of the carriers in the carrier pocket of material j in the wire coordinate system is then written as

$$E_j(k) = \frac{\hbar^2}{2} k \cdot \alpha_j \cdot k + V_j, \tag{2.3}$$

where

$$\alpha_j \equiv M_{wire,j}^{-1} = \begin{pmatrix} \alpha_{11,j} & \alpha_{12,j} & \alpha_{13,j} \\ \alpha_{12,j} & \alpha_{22,j} & \alpha_{23,j} \\ \alpha_{13,j} & \alpha_{23,j} & \alpha_{33,j} \end{pmatrix} \tag{2.4}$$

is the inverse mass tensor of material j in the wire coordinate system and V_j is the potential energy of the carriers of material j. In general, one of the V_j is set to be zero for a single pocket for the core and a single pocket for the shell core-shell nanowire system. From the effective mass theorem [11], the envelope wavefunction of carriers of material j, $\Psi_j(r,\theta)$, is solved through the Schrödinger equation,

$$-\frac{\hbar^2}{2} \nabla \cdot \alpha_j \cdot \nabla \Psi_j(r,\theta) + V_j \Psi_j(r,\theta) = E_j \Psi_j(r,\theta). \tag{2.5}$$

Equation (2.5) is obtained by replacing k with $(-i\nabla)$ in Equation (2.3).

Using Equation (2.5) and the assumptions stated in Section 2.1, the Schrödinger equations for the carriers of material A and of material B in the core-shell nanowire are found to be

$$-\frac{\hbar^2}{2} \nabla \cdot \alpha_A \cdot \nabla \Psi_A(r,\theta) + V_A \Psi_A(r,\theta) = E \Psi_A(r,\theta) \qquad \text{for the core region,}$$

and

$$-\frac{\hbar^2}{2} \nabla \cdot \alpha_B \cdot \nabla \Psi_B(r,\theta) + V_B \Psi_B(r,\theta) = E \Psi_B(r,\theta) \qquad \text{for the shell region,} \tag{2.6}$$

where the potential offset at the interface between the two materials is given by $V = V_B - V_A$. Together, $\Psi_A(r,\theta)$ and $\Psi_B(r,\theta)$ form the wavefunction $\Psi(r,\theta)$ for the core-shell nanowire system where A denotes the core region and B denotes the shell region. Following from the basic continuity requirements of wave functions and their derivatives at the boundaries, we get $\Psi_A(r = d/2, \theta) = \Psi_B(r = d/2, \theta)$ and $\frac{\partial}{\partial r}\Psi_A(r = d/2, \theta) = \frac{\partial}{\partial r}\Psi_B(r = d/2, \theta)$ at the materials' interface. At the same time, $\Psi(r,\theta)$ is also assumed to vanish at the outer interface in this core-shell nanowire model.

By setting $V_A = 0$ as the reference energy, Equation (2.6) becomes

$$\left(-\frac{\hbar^2}{2} \nabla \cdot \alpha_A \cdot \nabla\right) \Psi(r,\theta) = E\Psi(r,\theta) \qquad \text{for the core region,}$$

and

$$\left(-\frac{\hbar^2}{2} \nabla \cdot \alpha_B \cdot \nabla + V\right) \Psi(r,\theta) = E\Psi(r,\theta) \qquad \text{for the shell region.} \tag{2.7}$$

Equation (2.7) can be further simplified by applying the symmetry properties of the core-shell nanowire. Due to the wire's cylindrical symmetry, all its physical properties are invariant under rotation about the z axis. By applying a proper rotation about the z axis, the off-diagonal matrix elements $\alpha_{12,j}$ can be made to be equal to 0. With $\alpha_{12,j} = 0$, Equation (2.7) can be rewritten as

$$\begin{aligned} & \alpha_{11,A}\frac{\partial^2}{\partial x^2}\Psi + \alpha_{22,A}\frac{\partial^2}{\partial y^2}\Psi + \alpha_{33,A}\frac{\partial^2}{\partial z^2}\Psi + 2\alpha_{13,A}\frac{\partial^2}{\partial x \partial z}\Psi + 2\alpha_{23,A}\frac{\partial^2}{\partial y \partial z}\Psi \\ = & \left(-\frac{2E}{\hbar^2}\right)\Psi \\ & \text{for the core region,} \end{aligned}$$

and

$$\begin{aligned} & \alpha_{11,B}\frac{\partial^2}{\partial x^2}\Psi + \alpha_{22,B}\frac{\partial^2}{\partial y^2}\Psi + \alpha_{33,B}\frac{\partial^2}{\partial z^2}\Psi + 2\alpha_{13,B}\frac{\partial^2}{\partial x \partial z}\Psi + 2\alpha_{23,B}\frac{\partial^2}{\partial y \partial z}\Psi \\ = & \left(-\frac{2(E-V)}{\hbar^2}\right)\Psi \\ & \text{for the shell region.} \end{aligned} \tag{2.8}$$

In the core-shell nanowire, the carriers are unbounded in the wire direction, but are bounded in the x and y directions. As a result, the envelope wavefunction of the carriers can be written as a product of a traveling wave in the z direction and a bound-state wavefunction in the x and y directions for each region, such as,

$$\Psi(r,\theta) = \begin{cases} u(x,y)\exp(ik_{x,A}x)\exp(ik_{y,A}y)\exp(ik_{z,A}z) & \text{for the core region,} \\ v(x,y)\exp(ik_{x,B}x)\exp(ik_{y,B}y)\exp(ik_{z,B}z) & \text{for the shell region,} \end{cases} \tag{2.9}$$

where $k_{x,j}$ and $k_{y,j}$ are the wavevectors in the x and y directions in medium j, and $k_{z,j}$ is the wavevector of the traveling wave in the z direction in medium j. Substituting Equation (2.9) into Equation (2.8) results in

$$\begin{aligned}\alpha_{11,A}\tfrac{\partial^2 u}{\partial x^2} + \alpha_{22,A}\tfrac{\partial^2 u}{\partial y^2} + 2i(\alpha_{11,A}k_{x,A} + \alpha_{13,A}k_{z,A})\tfrac{\partial u}{\partial x} \\ +2i(\alpha_{22,A}k_{y,A} + \alpha_{23,A}k_{z,A})\tfrac{\partial u}{\partial y} = -\tfrac{2E}{\hbar^2}u \\ +(\alpha_{11,A}k_{x,A}^2 + \alpha_{22,A}k_{y,A}^2 + \alpha_{33,A}k_{z,A}^2 + 2\alpha_{13,A}k_{x,A}k_{z,A} + 2\alpha_{23,A}k_{y,A}k_{z,A})u \\ \text{for the core region,}\end{aligned}$$

and

$$\begin{aligned}\alpha_{11,B}\tfrac{\partial^2 v}{\partial x^2} + \alpha_{22,B}\tfrac{\partial^2 v}{\partial y^2} + 2i(\alpha_{11,B}k_{x,B} + \alpha_{13,B}k_{z,B})\tfrac{\partial v}{\partial x} \\ +2i(\alpha_{22,B}k_{y,B} + \alpha_{23,B}k_{z,B})\tfrac{\partial v}{\partial y} = -\tfrac{2(E-V)}{\hbar^2}v \\ +(\alpha_{11,B}k_{x,B}^2 + \alpha_{22,B}k_{y,B}^2 + \alpha_{33,B}k_{z,B}^2 + 2\alpha_{13,B}k_{x,B}k_{z,B} + 2\alpha_{23,B}k_{y,B}k_{z,B})v \\ \text{for the shell region.}\end{aligned} \tag{2.10}$$

By selecting $k_{x,j} = -(\alpha_{13,j}/\alpha_{11,j})k_{z,j}$ and $k_{y,j} = -(\alpha_{23,j}/\alpha_{11,j})k_{z,j}$, the coupling imaginary terms are eliminated. This procedure is merely choosing a phase factor for the function in the x and y directions so that Equation (2.10) becomes a simpler equation to deal with. This phase selection is only for mathematical convenience and it does not alter the physical properties considered in Equation (2.10) since the quantity of interest is $|\Psi(r,\theta)|^2$ instead of $\Psi(r,\theta)$. With the imaginary terms eliminated, Equation (2.10) becomes a simple second-order differential equation of the form,

$$-\frac{\hbar^2}{2}\left(\alpha_{11,A}\frac{\partial^2}{\partial x^2} + \alpha_{22,A}\frac{\partial^2}{\partial y^2}\right)u = \left(E - \frac{\hbar^2 k_{z,A}^2}{2m_{33,A}}\right)u \qquad \text{for the core region,}$$

and

$$-\frac{\hbar^2}{2}\left(\alpha_{11,B}\frac{\partial^2}{\partial x^2} + \alpha_{22,B}\frac{\partial^2}{\partial y^2}\right)v = \left(E - V - \frac{\hbar^2 k_{z,B}^2}{2m_{33,B}}\right)v \quad \text{for the shell region,} \tag{2.11}$$

where

$$m_{33,j} \equiv (\alpha_{33,j} - \frac{\alpha_{23,j}^2}{\alpha_{22,j}} - \frac{\alpha_{13,j}^2}{\alpha_{11,j}})^{-1} = \hat{z} \cdot M_{wire,j} \cdot \hat{z}. \tag{2.12}$$

Equation (2.11) is nothing but a 2D Schrödinger equation with effective masses

$$\begin{aligned} m_{x,j} &\equiv \alpha_{11,j}^{-1} = (\hat{x}' \cdot M_{wire,j}^{-1} \cdot \hat{x})^{-1} \\ m_{y,j} &\equiv \alpha_{22,j}^{-1} = (\hat{y}' \cdot M_{wire,j}^{-1} \cdot \hat{y})^{-1} \end{aligned} \tag{2.13}$$

in the x and y directions, respectively. Similar to the infinite square well problem, the wavefunction $\Psi(r,\theta)$, or equivalently $u(x,y)$, vanishes at the boundary (outer interface of the core-shell nanowire), resulting in the quantization of the carrier energies of the core-shell nanowire system. However, because of the 2D confinement in the core-shell nanowire system, two different indices, labeled as n and m, are needed. Thus, the energies of the core-shell nanowire system become

$$E_{n,m}(k_{z,j}) = \epsilon_{n,m} + \frac{\hbar^2 k_{z,j}^2}{2m_{33,j}}, \tag{2.14}$$

where $\epsilon_{n,m}$ is the eigenvalue of Equation (2.11) when $k_{z,j} = 0$. At a first glance, the quantity $k_{z,j}$ seems to be both material dependent and pocket dependent. However, since all the calculations are done in the wire coordinates, $k_{z,j}$ is indeed the same as the global wavevector k_z. From Equation (2.14), one sees that the carrier states split into many subbands with band edge energies $\epsilon_{n,m}$, and each subband behaves like a 1D free electron in the z direction with an effective mass $m_z = m_{33,j}$. Here $\epsilon_{n,m}$ denotes the stationary band edge energy of the system, whereas $\hbar^2 k_{z,j}^2/(2m_{33,j})$ denotes the kinetic energy of the carriers in the z direction. One should note that the effective masses $m_{x,j}$ and $m_{y,j}$ that determine the bound-state energies have different expressions from the transport effective mass $m_{z,j}$ that characterizes the 1D dispersion relation (see Equation (2.12) and Equation(2.13)). As a reminder, the above formalism has only considered the case for a single pocket core and a single pocket shell core-shell nanowire system. For a multiple pocket core-shell nanowire system, each of the pocket-pairs is considered using the above formalism with one common global reference energy. The effect of each of the pocket-pair is combined together in the end using the global reference energy and a global wavevector system, and the relationship between $E(k)$ and k could then be obtained.

2.3 Numerical Solution to the Core-Shell Schrödinger Equation

In Section 2.2, the 3D core-shell nanowire Schrödinger equation was simplified to an equivalent 2D differential equation. Due to the free electron behavior of the carriers in the z direction, the carriers can have any positive amount of energy associated with them. Therefore, the quantities of interest are the band edge energies of all the subbands, $\epsilon_{n,m}$, instead of the total energy, $E_{n,m}$. Here $\epsilon_{n,m}$ is obtained by solving Equation (2.11) with the condition $k_{z,A} = k_{z,B} = 0$. By setting $k_{z,A} = k_{z,B} = 0$, Equation (2.11) can be rewritten in a more compact form as follows,

$$\left(\alpha_{11,A}\frac{\partial^2}{\partial x^2} + \alpha_{22,A}\frac{\partial^2}{\partial y^2}\right) u = -\lambda u \qquad \text{for the core region,}$$

and

$$\left(\alpha_{11,B}\frac{\partial^2}{\partial x^2} + \alpha_{22,B}\frac{\partial^2}{\partial y^2}\right) v = \left(-\lambda + V'\right) v \qquad \text{for the shell region,} \tag{2.15}$$

where

$$\lambda \equiv \frac{2E}{\hbar^2} = \frac{2\epsilon}{\hbar^2}, \tag{2.16}$$

and

$$V' \equiv \frac{2V}{\hbar^2}. \tag{2.17}$$

In general, the α's in Equation (2.15) are different and the V' is nonzero, leading to a non-analytic solution for Equation (2.15). In the following, a numerical scheme is applied to solve this differential equation. With the aid of numerical simulations, accurate solutions for Equation (2.15) could be obtained.

Recalling that for a core-shell nanowire with a core diameter d and with a total core-shell diameter e, the boundary conditions for the wavefunctions $u(x, y)$ and $v(x, y)$ when $k_{z,A} = k_{z,B} = 0$ are

$$\begin{aligned} &u(x,y) = v(x,y) && \text{at}\, r = d/2, \\ &\frac{\partial}{\partial r}u(x,y) = \frac{\partial}{\partial r}v(x,y) && \text{at}\, r = d/2, \\ &v(x,y) = 0 && \text{at}\, r = e/2. \end{aligned} \tag{2.18}$$

Since the core-shell nanowire has a cylindrical symmetry and its boundary conditions are expressed in terms of cylindrical coordinates, it would be best to work in cylindrical coordinates. Using a cylindrical symmetry transformation [10], Equation (2.15) becomes

$$\begin{aligned}
& \alpha_{11,A}\left(\cos^2\theta\frac{\partial^2 u}{\partial r^2}+2\frac{\cos\theta\sin\theta}{r^2}\frac{\partial u}{\partial\theta}-2\frac{\cos\theta\sin\theta}{r}\frac{\partial^2 u}{\partial r\partial\theta}+\frac{\sin^2\theta}{r}\frac{\partial u}{\partial r}+\frac{\sin^2\theta}{r^2}\frac{\partial^2 u}{\partial\theta^2}\right)\\
+\quad & \alpha_{22,A}\left(\sin^2\theta\frac{\partial^2 u}{\partial r^2}-2\frac{\cos\theta\sin\theta}{r^2}\frac{\partial u}{\partial\theta}+2\frac{\cos\theta\sin\theta}{r}\frac{\partial^2 u}{\partial r\partial\theta}+\frac{\cos^2\theta}{r}\frac{\partial u}{\partial r}+\frac{\cos^2\theta}{r^2}\frac{\partial^2 u}{\partial\theta^2}\right)\\
=\quad & \hfill -\lambda u
\end{aligned}$$

for the core region,

and

$$\begin{aligned}
& \alpha_{11,B}\left(\cos^2\theta\frac{\partial^2 v}{\partial r^2}+2\frac{\cos\theta\sin\theta}{r^2}\frac{\partial v}{\partial\theta}-2\frac{\cos\theta\sin\theta}{r}\frac{\partial^2 v}{\partial r\partial\theta}+\frac{\sin^2\theta}{r}\frac{\partial v}{\partial r}+\frac{\sin^2\theta}{r^2}\frac{\partial^2 v}{\partial\theta^2}\right)\\
+\quad & \alpha_{22,B}\left(\sin^2\theta\frac{\partial^2 v}{\partial r^2}-2\frac{\cos\theta\sin\theta}{r^2}\frac{\partial v}{\partial\theta}+2\frac{\cos\theta\sin\theta}{r}\frac{\partial^2 v}{\partial r\partial\theta}+\frac{\cos^2\theta}{r}\frac{\partial v}{\partial r}+\frac{\cos^2\theta}{r^2}\frac{\partial^2 u}{\partial\theta^2}\right)\\
=\quad & \hfill (-\lambda+V')v
\end{aligned}$$

for the shell region,

(2.19)

where θ is the polar angle from the x axis and r is the distance from the origin of the $x-y$ plane of the core-shell nanowire in cylindrical coordinates. To transform Equation (2.19) into a difference equation, a set of points is created in the x-y plane of the core-shell nanowire. Since the problem has been transformed into polar coordinates, it is natural to assign the grid points according to cylindrical coordinates θ and r. The diameter of the core-shell nanowire e is divided into M equal segments δr, while the angular coordinate θ of the wire in the $x-y$ plane, which includes a range of 2π, is divided into N equal segments $\delta\theta$. This assignment is equivalent to dividing the $x-y$ plane of the core-shell nanowire into M concentric circles that are δr apart from each other, and N equivalent pieces subtending an angle of $\delta\theta$ (see Figure 2-2). This assignment of the grid points results in a total of $M \times N$ grid points in the $x-y$

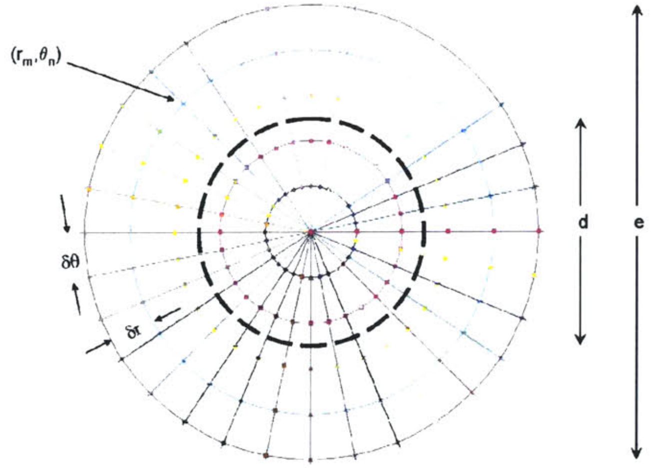

Figure 2-2: A schematic view of the grid points in the $x - y$ plane of the core-shell nanowire. $M = 5$, $N = 32$, and $m' = 2$ for this special case.

plane of the core-shell nanowire and the polar coordinates of the grid points are

$$(r_m, \theta_n) = (m\delta r, n\delta\theta), \qquad \begin{array}{l} m = 1, 2, \ldots, m', m'+1, \ldots, M \\ n = 0, 1, \ldots, (N-1) \end{array} \tag{2.20}$$

where $\delta r = e/(2M)$ and $\delta\theta = 2\pi/N$ are the distances between adjacent circles and the angular segment of each piece, respectively. The grid points with index $1 \leq m \leq m'$ lie in the core region, whereas those with $m' < m \leq M$ lie in the shell region. It should be noted that due to the cylindrical symmetry, grid point (r_m, θ_{-k}) and (r_m, θ_{N-k}) represent the same point.

One might want to consider an adaptive grid for this core-shell nanowire system due to the difference in the size of the core and the size of the shell. However, the generation of an adaptive grid is usually used when the difference between different parts of the solution is enormous, such as on the order of 10th to 20th orders of magnitude difference. In the present case, where different parts of the solution do not differ much, a uniform grid will result in a much more simple problem to solve and a much more accurate solution [12].

Using a three point center differencing scheme, the derivatives in Equation (2.19) can be approximated by

$$\begin{aligned}
\left[\frac{\partial u}{\partial r}\right]_{m,n} &= \frac{u_{m+1,n} - u_{m-1,n}}{2\delta r} - \frac{(\delta r)^2}{3!}\left[\frac{\delta^3 u}{\delta r^3}\right]_{m,n} + \dots, \\
\left[\frac{\partial u}{\partial \theta}\right]_{m,n} &= \frac{u_{m+1,n} - u_{m-1,n}}{2\delta \theta} - \frac{(\delta \theta)^2}{3!}\left[\frac{\delta^3 u}{\delta \theta^3}\right]_{m,n} + \dots, \\
\left[\frac{\partial^2 u}{\partial r^2}\right]_{m,n} &= \frac{u_{m+1,n} - 2u_{m,n} + u_{m-1,n}}{(\delta r)^2} - \frac{(\delta r)^2}{12}\left[\frac{\delta^4 u}{\delta r^4}\right]_{m,n} + \dots, \\
\left[\frac{\partial^2 u}{\partial \theta^2}\right]_{m,n} &= \frac{u_{m+1,n} - 2u_{m,n} + u_{m-1,n}}{(\delta \theta)^2} - \frac{(\delta \theta)^2}{12}\left[\frac{\delta^4 u}{\delta \theta^4}\right]_{m,n} + \dots, \\
\left[\frac{\partial^2 u}{\partial r \partial \theta}\right]_{m,n} &= \frac{(u_{m+1,n+1} - u_{m+1,n-1}) - (u_{m-1,n+1} - u_{m-1,n-1})}{4(\delta\theta)(\delta r)} \\
&\quad + O((\delta r)^2) + O((\delta\theta)^2) + \dots,
\end{aligned} \tag{2.21}$$

where $u_{m,n} = u(r_m, \theta_n)$ is the value of the wavefunction $u(r, \theta)$ at the grid point $r = r_m$ and $\theta = \theta_n$. Note that the leading error terms for all of the derivatives are proportional to either $(\delta r)^2$ or $(\delta\theta)^2$. Thus, as the spacing between the grid points get smaller, the error becomes smaller quadratically. A more accurate scheme can be obtained by using a higher order center differencing scheme for the derivatives. Substituting Equation (2.21) into Equation (2.19), a finite difference equation is obtained and it has the form

$$\begin{aligned}\lambda u_{m,n} = \quad & A_{m,n,A}u_{m+1,n} + B_{m,n,A}u_{m-1,n} + C_{m,n,A}u_{m,n+1} + D_{m,n,A}u_{m,n-1} \\ & +E_{m,n,A}(u_{m+1,n+1} + u_{m-1,n-1} - u_{m-1,n+1} - u_{m+1,n-1}) + F_{m,n}u_{m,n} \\ & \text{for the core region,}\end{aligned}$$

and

$$\begin{aligned}\lambda v_{m,n} = \quad & A_{m,n,B}v_{m+1,n} + B_{m,n,B}v_{m-1,n} + C_{m,n,B}v_{m,n+1} + D_{m,n,B}v_{m,n-1} \\ & +E_{m,n,B}(v_{m+1,n+1} + v_{m-1,n-1} - v_{m-1,n+1} - v_{m+1,n-1}) + G_{m,n}v_{m,n} \\ & \text{for the shell region,} \qquad (2.22)\end{aligned}$$

where

$$\begin{aligned}A_{m,n,j} &= -\frac{\alpha_{11,j}}{\delta r}\left(\frac{cos^2\theta_n}{\delta r} + \frac{sin^2\theta_n}{2r_m}\right) - \frac{\alpha_{22,j}}{\delta r}\left(\frac{sin^2\theta_n}{\delta r} + \frac{cos^2\theta_n}{2r_m}\right), \\ B_{m,n,j} &= -\frac{\alpha_{11,j}}{\delta r}\left(\frac{cos^2\theta_n}{\delta r} - \frac{sin^2\theta_n}{2r_m}\right) - \frac{\alpha_{22,j}}{\delta r}\left(\frac{sin^2\theta_n}{\delta r} - \frac{cos^2\theta_n}{2r_m}\right), \\ C_{m,n,j} &= -\frac{\alpha_{11,j}sin\theta_n}{r_m^2\delta\theta}\left(cos\theta_n + \frac{sin\theta_n}{\delta\theta}\right) - \frac{\alpha_{22,j}cos\theta_n}{r_m^2\delta\theta}\left(-sin\theta_n + \frac{cos\theta_n}{\delta\theta}\right), \\ D_{m,n,j} &= -\frac{\alpha_{11,j}sin\theta_n}{r_m^2\delta\theta}\left(-cos\theta_n + \frac{sin\theta_n}{\delta\theta}\right) - \frac{\alpha_{22,j}cos\theta_n}{r_m^2\delta\theta}\left(sin\theta_n + \frac{cos\theta_n}{\delta\theta}\right), \\ E_{m,n,j} &= -\frac{sin\theta_n cos\theta_n}{2r_m\delta\theta\delta r}\left(-\alpha_{11,j} + \alpha_{22,j}\right), \\ F_{m,n} &= 2\alpha_{11,A}\left(\frac{cos^2\theta_n}{(\delta r)^2} + \frac{sin^2\theta_n}{r_m^2(\delta\theta)^2}\right) + 2\alpha_{22,A}\left(\frac{sin^2\theta_n}{(\delta r)^2} + \frac{cos^2\theta_n}{r_m^2(\delta\theta)^2}\right), \\ G_{m,n} &= 2\alpha_{11,B}\left(\frac{cos^2\theta_n}{(\delta r)^2} + \frac{sin^2\theta_n}{r_m^2(\delta\theta)^2}\right) + 2\alpha_{22,B}\left(\frac{sin^2\theta_n}{(\delta r)^2} + \frac{cos^2\theta_n}{r_m^2(\delta\theta)^2}\right) + V'. \qquad (2.23)\end{aligned}$$

There is one difference equation for each grid point (r_m, θ_n) on the core-shell nanowire, resulting in a total of $M \times N$ equations for the $M \times N$ grid points.

Special care is needed when dealing with the grid points at the center, at the outer interface, and near the core-shell interface. Using one of the boundary conditions, the grid points at the outer interface are required to be zero, namely, $v_{M,n} = 0$. This boundary condition decreases the number of grid points (equivalently, the number of difference equations) from $M \times N$ to $(M-1) \times N$. For the case of the grid points at the center, the u can be approximated as [10]

$$\begin{aligned} u_{0,n} = u_{0,0} &= \frac{\alpha_{11,A}(u_{1,0} + u_{1,\pi}) + \alpha_{22,A}(u_{1,\pi/2} + u_{1,3\pi/2})}{-(\delta r)^2 \lambda + 2(\alpha_{11,A} + \alpha_{22,A})} \\ &\approx \frac{\alpha_{11,A}(u_{1,0} + u_{1,\pi}) + \alpha_{22,A}(u_{1,\pi/2} + u_{1,3\pi/2})}{2(\alpha_{11,A} + \alpha_{22,A})} \end{aligned} \tag{2.24}$$

with the condition

$$(\delta r)^2 \ll \frac{2(\alpha_{11,A} + \alpha_{22,A})}{\lambda}. \tag{2.25}$$

As for the region near the core-shell interface, the values of u and v just next to the interface are extended to the next region and assumed to be approximately equal to the values in the other region, namely, $u_{m',n} = v_{m',n}$ and $u_{m'+1,n} = v_{m'+1,n}$. It should be noted that $u_{m'+1,n}$ and $v_{m',n}$ do not actually exist, but they are required as a by-product of the three point center differencing scheme. Using these boundary conditions at the interface, Equation (2.22) for $m = m'$ (=2 for the case in Figure 2-2) and $m = m' + 1$ (=3 for the case in Figure 2-2) results in

$$\begin{aligned} \lambda u_{m',n} = \quad & A_{m',n,A} v_{m'+1,n} + B_{m',n,A} u_{m'-1,n} + C_{m',n,A} u_{m',n+1} + D_{m',n,A} u_{m,n-1} \\ & + E_{m',n,A}(v_{m'+1,n+1} + u_{m'-1,n-1} - v_{m'+1,n-1} - u_{m'-1,n+1}) + F_{m',n} u_{m',n} \\ & \text{for}\, m = m', \end{aligned}$$

and

$$\begin{aligned} \lambda v_{m'+1,n} = \quad & A_{m'+1,n,B} v_{m'+2,n} + B_{m'+1,n,B} u_{m',n} + C_{m'+1,n,B} v_{m'+1,n+1} + D_{m'+1,n,B} v_{m'+1,n-1} \\ & + E_{m'+1,n,B}(v_{m'+2,n+1} + u_{m',n-1} - v_{m'+2,n-1} - u_{m',n+1}) + G_{m'+1,n} v_{m'+1,n} \\ & \text{for}\, m = m' + 1. \end{aligned} \tag{2.26}$$

Taking these special cases into considerations, the $(M-1) \times N$ difference equation can be expressed in a matrix form

$$\begin{pmatrix} H_{(1,0)(1,0)} & \cdots & H_{(1,0)(m',0)} & \cdots & H_{(1,0)(M-1,N-1)} \\ H_{(1,1)(1,0)} & \cdots & H_{(1,1)(m',0)} & \cdots & H_{(1,1)(M-1,N-1)} \\ \vdots & & & & \vdots \\ \vdots & & & & \vdots \\ H_{(m',0)(1,0)} & & & & H_{(m',0)(M-1,N-1)} \\ \vdots & & \hat{H} & & \vdots \\ H_{(m'+1,0)(1,0)} & & & & H_{(m'+1,0)(M-1,N-1)} \\ \vdots & & & & \vdots \\ \vdots & & & & \vdots \\ H_{(M-1,N-2)(1,0)} & \cdots & H_{(M-1,N-2)(m',0)} & \cdots & H_{(M-1,N-2)(M-1,N-1)} \\ H_{(M-1,N-1)(1,0)} & \cdots & H_{(M-1,N-1)(m',0)} & \cdots & H_{(M-1,N-1)(M-1,N-1)} \end{pmatrix}$$

$$\times \begin{pmatrix} u_{1,0} \\ u_{1,1} \\ \vdots \\ u_{1,N-1} \\ u_{2,0} \\ \vdots \\ u_{m',0} \\ \vdots \\ u_{m',N-1} \\ v_{m'+1,0} \\ v_{m'+1,1} \\ \vdots \\ v_{m'+1,N-1} \\ v_{m'+2,0} \\ \vdots \\ v_{M-1,N-1} \end{pmatrix} = \lambda \begin{pmatrix} u_{1,0} \\ u_{1,1} \\ \vdots \\ u_{1,N-1} \\ u_{2,0} \\ \vdots \\ u_{m',0} \\ \vdots \\ u_{m',N-1} \\ v_{m'+1,0} \\ v_{m'+1,1} \\ \vdots \\ v_{m'+1,N-1} \\ v_{m'+2,0} \\ \vdots \\ v_{M-1,N-1} \end{pmatrix} \qquad (2.27)$$

where $\hat{H}$ is obtained from Equation (2.22). As an illustration, the determination of the coefficient $H_{(1,0)(1,0)}$ is presented in this section. Applying Equation (2.22) for the grid point $(r_1, \theta_0) = (\delta r, 0)$ results in

$$\begin{aligned}\lambda u_{1,0} &= A_{1,0,A} u_{2,0} + B_{1,0,A} u_{0,0} + C_{1,0,A} u_{1,1} + D_{1,0,A} u_{1,-1} \\ &\quad + E_{1,0,A}(u_{2,1} + u_{0,-1} - u_{0,1} - u_{2,-1}) + F_{1,0} u_{1,0} \\ &= A_{1,0,A} u_{2,0} + B_{1,0,A} u_{0,0} + C_{1,0,A} u_{1,1} + D_{1,0,A} u_{1,N-1} \\ &\quad + E_{1,0,A}(u_{2,1} - u_{2,N-1}) + F_{1,0} u_{1,0}.\end{aligned} \tag{2.28}$$

Substituting Equation (2.24) into Equation (2.28), the coefficient $H_{(1,0)(1,0)}$ is found to be

$$H_{(1,0)(1,0)} = B_{1,0} \frac{\alpha_{11,A}}{2(\alpha_{11,A} + \alpha_{22,A})} + F_{1,0}. \tag{2.29}$$

With all the $\hat{H}$ coefficients readily available, the u, v, and λ in Equation (2.27) can be solved easily with the aid of software such as Matlab or Mathematica. As a reminder, it should be noted that the approximation made for $u_{0,n}$ assumed the condition $(\delta r)^2 \ll 2(\alpha_{11,A} + \alpha_{22,A})/\lambda$, and the use of a uniform grid assumes that the solutions $\Psi(r, \theta)$ do not change rapidly (low energy states). Thus, the accuracy of the solution decreases as the eigenvalue (eigen-energy) increases.

Table 2.1: Comparison of the lowest four eigenvalues $\lambda_{\text{core-shell wire}}$ and $\lambda_{\text{simple wire}}$ and their degeneracies for the special case of $\alpha_{11,A} = \alpha_{22,A} = \alpha_{11,B} = \alpha_{22,B} = 1$.

$\lambda_{\text{core-shell wire}}$	$\lambda_{\text{simple wire}}$	Degeneracy
5.7837	5.7837	1
14.6688	14.6688	2
26.2624	26.2624	2
30.4678	30.4678	1

2.4 Comparison with the Nanowire Numerical Solution

The core-shell nanowire numerical solution obtained in this thesis is compared with the previously published simple nanowire calculation [10]. The cases and parameters are selected accordingly to the conditions of the previously published results. When the core and the shell material of the core-shell nanowire have the same effective mass tensor and the same crystallographic orientation along with a zero interface offset, the case of a core-shell nanowire reduces to the case of a simple nanowire. Table 2.1 compares the lowest four eigenvalues $\lambda_{\text{core-shell wire}}$ and $\lambda_{\text{simple wire}}$ and their degeneracies for the special case of $\alpha_{11,A} = \alpha_{22,A} = \alpha_{11,B} = \alpha_{22,B} = 1$. Table 2.2 compares the lowest four eigenvalues $\lambda_{\text{core-shell wire}}$ and $\lambda_{\text{simple wire}}$ for the special case of $\alpha_{11,A} = \alpha_{11,B} = 1$ and $\alpha_{22,A} = \alpha_{22,B} = 3$. All the values in these tables are computed under the condition where $d = 1\,\text{nm}$, $e = 2\,\text{nm}$, $V = 0\,\text{eV}$, $M = 64$, and $N = 40$. The results show that the core-shell nanowire numerical scheme gives exactly the same result as the nanowire numerical scheme. This agreement provides some check on the computer program used to calculate the results for the core-shell nanowire model.

Table 2.2: Comparison of the lowest four eigenvalues $\lambda_{\text{core-shell wire}}$ and $\lambda_{\text{simple wire}}$ and their degeneracies for the special case of $\alpha_{11,A} = \alpha_{11,B} = 1$ and $\alpha_{22,A} = \alpha_{22,B} = 3$.

$\lambda_{\text{core-shell wire}}$	$\lambda_{\text{simple wire}}$	Degeneracy
11.4759	11.4759	1
21.7205	21.7205	1
36.2447	36.2447	1
36.2874	36.2874	1

Chapter 3

Modeling of the Si/SiGe Core-Shell Nanowire

This chapter first presents the properties of Si, Ge, and SiGe, along with the effect of strain on SiGe in Section 3.1. It then continues with the approximations and assumptions used for modeling the Si/SiGe core-shell nanowire structure in Section 3.2. The chapter concludes with the effect of different parameters on the system in Section 3.3.

3.1 Background

3.1.1 Properties of Si (Band Structure and Crystal Structure)

Si is a group IV semiconductor material. It has a diamond/zincblende crystal structure and it has a FCC lattice with two atoms per basis. The lattice constant for Si is 5.43 Å. The lattice constant used here for the diamond structure is for the large unit cell which contains 8 Si atoms. This unit cell is also used for Ge and SiGe alloys in the following sections. Si has a density of 2.329 g/cm^3. It is an indirect gap material

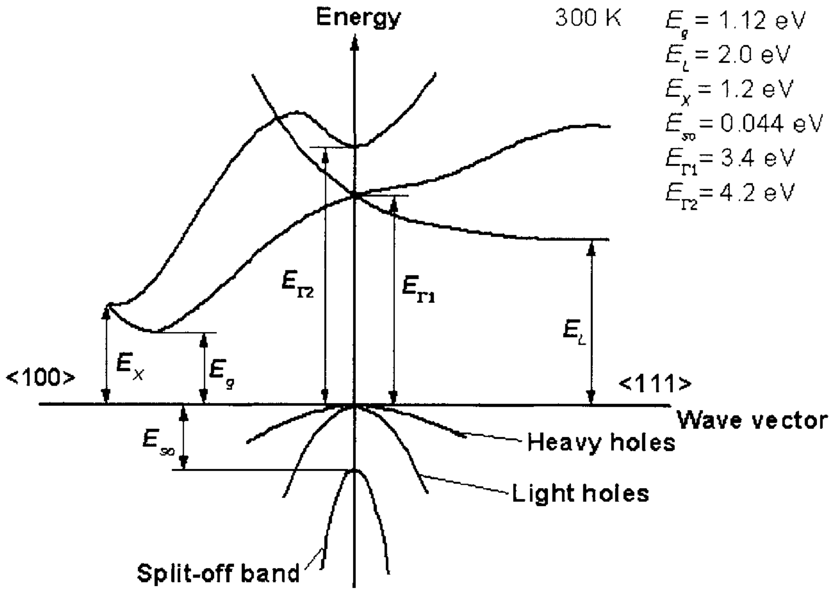

Figure 3-1: Band structure of Si [1].

with an indirect bandgap of 1.12 eV at room temperature [13].

Figure 3-1 shows the band structure of Si. Its conduction band is characterized by six equivalent ellipsoidal constant energy surface pockets with their minima located along the <100>-axes of the first Brillouin zone. The minima of these valleys are located at about $0.85k_0$ (Δ), where k_0 is the zone edge lattice vector from Γ (<000>) to X (<100>) as seen in Figure 3-1. The electron effective mass tensor of Si is given as

$$\begin{pmatrix} m_t & 0 & 0 \\ 0 & m_t & 0 \\ 0 & 0 & m_l \end{pmatrix}, \tag{3.1}$$

where the tensor is taken to have components along the three principal axes of each of the electronic pockets. m_t and m_l denote the transverse and longitudinal effective mass components, respectively. The longitudinal direction is along the principal axis where the pocket minima are located, and the two transverse directions are then along the other two principal axes. For example, an electron pocket with its energy minima located along [100] has its longitudinal axis as [100] and its transverse axes as [010] and [001]. At room temperature, m_t is $0.19m_0$ and m_l is $0.98m_0$ where m_0 is the electron rest mass [1].

On the other hand, the valence bands of Si are characterized by three spherical pockets (heavy hole, light hole, and split-off hole) with their maxima located at the zone center of the first Brillouin zone. The heavy hole and the light hole valence bands have a common energy extrema point. Due to the spin-orbit interaction, the split-off hole valence band pocket lies 0.044 eV below the other two valence bands at room temperature (300 K) (see Figure 3-1). Since all of the valence bands have spherical constant energy surfaces in the approximation used here, their masses are not direction dependent. The split-off valence band has an effective mass that is denoted by m_{so}. The heavy hole and light hole degenerate valence bands have an effective mass denoted by m_{hh} and m_{lh}, respectively. At room temperature, m_{hh} is $0.49m_0$, m_{lh} is $0.16m_0$, and m_{so} is $0.24m_0$ [1].

Due to its cubic symmetry, the mobility of bulk Si is isotropic. The mobility tensor for electrons in Si is given by

$$\begin{pmatrix} \mu_e & 0 & 0 \\ 0 & \mu_e & 0 \\ 0 & 0 & \mu_e \end{pmatrix}, \tag{3.2}$$

and the hole mobility tensor is given by

$$\begin{pmatrix} \mu_h & 0 & 0 \\ 0 & \mu_h & 0 \\ 0 & 0 & \mu_h \end{pmatrix}. \tag{3.3}$$

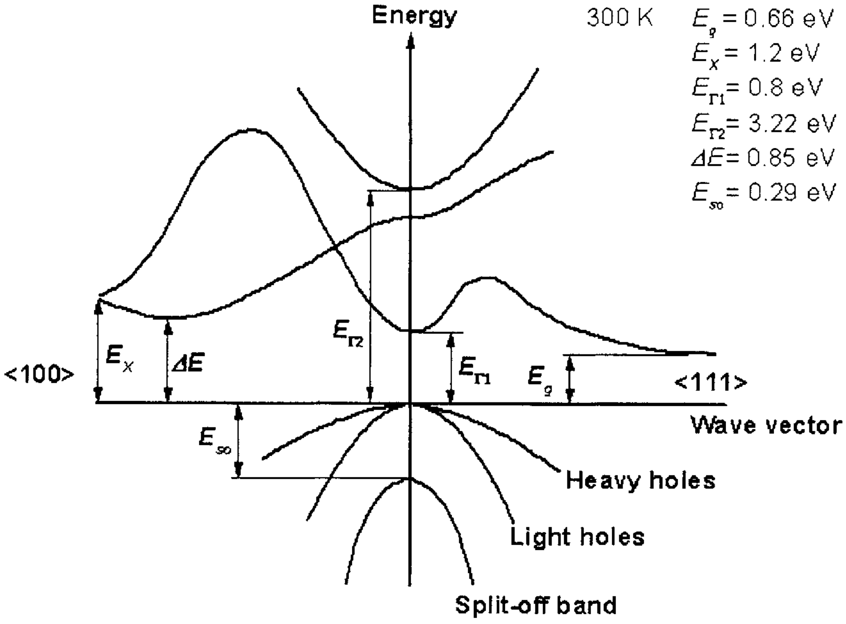

Figure 3-2: Band structure of Ge [2].

At room temperature, the intrinsic Si electron mobility and hole mobility is about 1400 $cm^2/(V \cdot s)$ and 450 $cm^2/(V \cdot s)$, respectively [1].

3.1.2 Properties of Ge (Band Structure and Crystal Structure)

Similar to Si, Ge is a group IV semiconductor material. It has a diamond/zincblende crystal structure. It also has a FCC lattice with two atoms per basis. The lattice constant for Ge is 5.658 Å. It has a density of 5.3234 g/cm^3. It is an indirect gap material with an indirect bandgap of 0.66 eV and a direct bandgap of 0.8 eV at room temperature (see Figure 3-2) [14].

Figure 3-2 shows the band structure of Ge. Its conduction band is characterized by four equivalent ellipsoidal constant energy surface pockets with their minima located about the L point where the <111>-axes intersect with the first Brillouin zone. The electron effective mass tensor of Ge is given as

$$\begin{pmatrix} m_t & 0 & 0 \\ 0 & m_t & 0 \\ 0 & 0 & m_l \end{pmatrix}, \tag{3.4}$$

where the tensor is expressed along the principal axes of each of the electronic pockets. m_t and m_l are the transverse and longitudinal effective mass components, respectively. The longitudinal direction is along the principal axis where the pocket minima are located, and the two transverse directions are then along the other two mutually orthogonal principal axes. For example, an electron pocket with its energy minima located along [111] has its longitudinal axis as [111] and its transverse axes as $[1\bar{1}0]$ and $[11\bar{2}]$. At room temperature, m_t is $0.0815m_0$ and m_l is $1.59m_0$ where m_0 is the electron rest mass [2].

On the other hand, the valence bands of Ge are characterized by three spherical pockets (heavy hole, light hole, and split-off hole) with their maxima located at the zone center of the first Brillouin zone. The heavy hole and the light hole valence bands have a common energy extrema point. Due to the spin-orbit interaction, the split-off hole valence band pocket lies 0.29 eV below the other two valence bands at room temperature (300 K) (see Figure 3-2). Since all of the valence bands have spherical constant energy surfaces in the approximation used here, their masses are not direction dependent. The split-off valence band has an effective mass that is denoted by m_{so}. The heavy hole and light hole degenerate valence bands have effective mass components labeled by m_{hh} and m_{lh}, respectively. At room temperature, m_{hh} is $0.33m_0$, m_{lh} is $0.043m_0$, and m_{so} is $0.084m_0$ [2].

Due to its cubic symmetry, the mobility of bulk Ge is isotropic. The mobility tensor for the electrons in Ge is given by

$$\begin{pmatrix} \mu_e & 0 & 0 \\ 0 & \mu_e & 0 \\ 0 & 0 & \mu_e \end{pmatrix}, \tag{3.5}$$

and the hole mobility tensor is given by

$$\begin{pmatrix} \mu_h & 0 & 0 \\ 0 & \mu_h & 0 \\ 0 & 0 & \mu_h \end{pmatrix}. \tag{3.6}$$

At room temperature, the intrinsic Ge electron mobility and hole mobility are about $3900\,cm^2/(V \cdot s)$ and $1900\,cm^2/(V \cdot s)$, respectively [2].

3.1.3 Properties of SiGe alloy (Band Structure and Crystal Structure)

SiGe forms a random alloy rather than a perfect crystal, since SiGe alloys do not have a periodic structure. However, the SiGe alloys possess properties that are very similar to those of Si or Ge, depending on the alloy composition [3]. To first order, the lattice constant of $\mathrm{Si}_{1-x}\mathrm{Ge}_x$ alloys (Figure 3-3) varies linearly from 5.43 Å to 5.658 Å with the Ge concentration x. Similar to both Si and Ge, the SiGe alloys have an indirect bandgap.

The band structure of the variation of the $\mathrm{Si}_x\mathrm{Ge}_{1-x}$ alloy with Si concentration x (Figure 3-4) shows a cross-over in its lowest conduction band edge from being located along <111> (Ge-like) for low Si concentrations to being located along <100> (Si-like) for larger Si concentrations. The crossover occurs at around $\mathrm{Si}_{0.15}\mathrm{Ge}_{0.85}$ for bulk samples, showing that for most of the range of Si concentration x, the band structure is Si-like. The effective mass and electronic behavior of the Si-like and the Ge-like

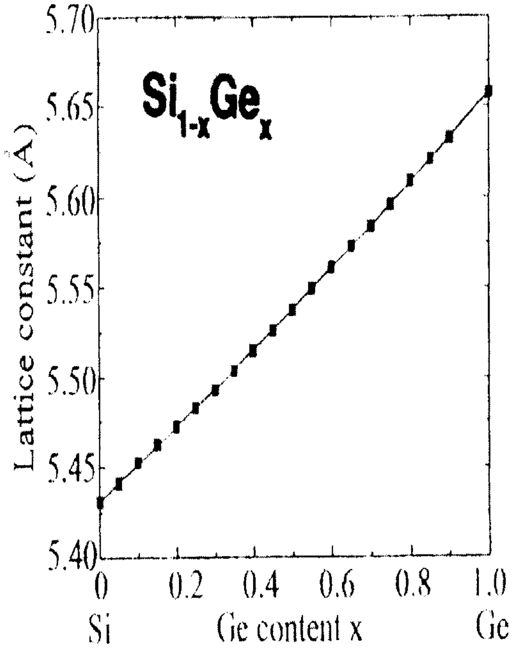

Figure 3-3: Lattice constant of Si$_{1-x}$Ge$_x$ alloys as a function of Ge content x. The lattice constants for pure Si and pure Ge are 5.43 Åand 5.658 Å, respectively [3].

SiGe alloys are approximately equivalent to those of Si and Ge, respectively.

The SiGe alloy has a lower mobility than pure Si or pure Ge for both the electrons and the holes (see Figure 3-5 and Figure 3-6). The hole mobility is lower than the electron mobility for Si, Ge, and SiGe alloys. The decrease in mobility in SiGe alloys relative to that for Si and Ge is mainly due to alloy carrier scattering. For electrons, near the cross-over composition $Si_{0.15}Ge_{0.85}$, intervalley electron scattering between the L point and the Δ point also plays a major role in decreasing the electron mobility.

3.1.4 Strain Effect on the SiGe Band Structure

There exists a rather large difference in the lattice constant between Si (5.43 Å) and Ge (5.658 Å), a 4.18 % difference. Due to this big lattice mismatch between Si and Ge, there is also a mismatch in the lattice constant between Si and SiGe alloys. Thus

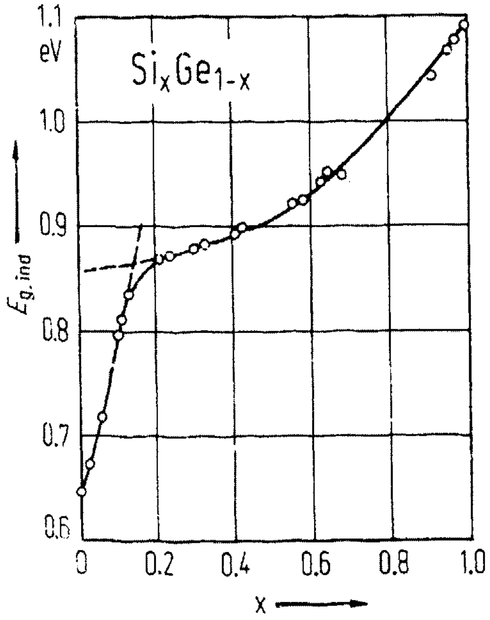

Figure 3-4: Indirect band gap of bulk SiGe alloys as a function of Si concentration. The cross over point occurs at about $Si_{0.15}Ge_{0.85}$. The band structure of Si (indirect band gap at a Δ point) persists over a wide range of Si concentrations. It is only for very high Ge concentrations (x < 0.15) that the indirect band gap is at the L point [4].

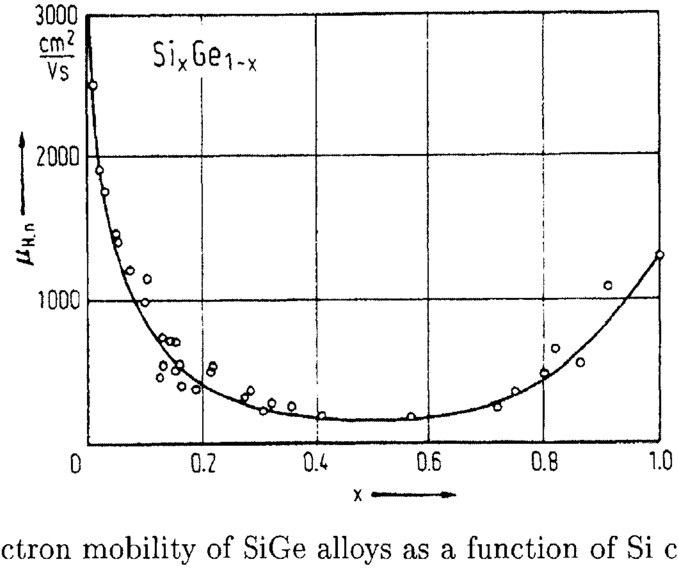

Figure 3-5: Electron mobility of SiGe alloys as a function of Si concentration [4].

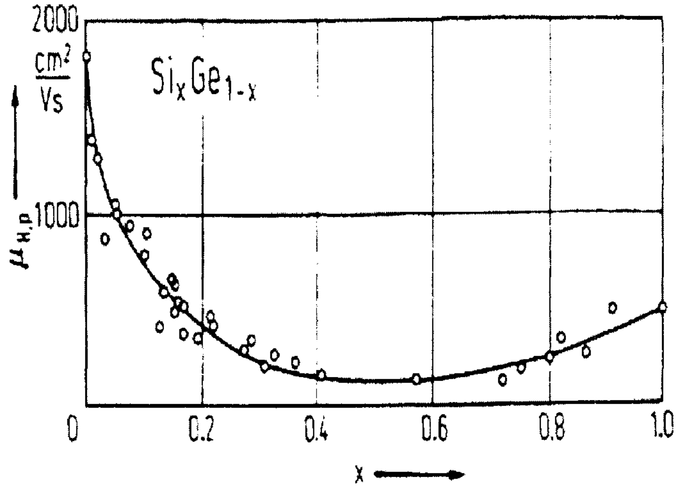

Figure 3-6: Hole mobility of SiGe alloys as a function of Si concentration [4].

misfit dislocations tend to be formed when a SiGe alloy is grown on a Si substrate. However, with advances in technology, it is now possible to grow a thin dislocation-free epitaxial layer of SiGe alloy on top of the Si substrate [15].

Because of the difference in lattice constants between Si and SiGe alloys, strain is introduced in the epitaxial SiGe alloy layer grown on top of a Si substrate, where the Si substrate in this case is regarded as a rigid body. This strain alters the electronic structure of the SiGe alloy layer.

Consider the case of a SiGe alloy 2D epitaxial layer grown on a Si substrate with a growth direction of [001] (labeled as the z axis) as an example. In this example, the SiGe alloy layer is under biaxial stress along [100] (labeled as the x axis), $[\bar{1}00]$ (labeled as the -x axis), [010] (labeled as the y axis), and $[0\bar{1}0]$ (labeled as the -y axis). This biaxial stress causes the in-plane (x and y) lattice constants of the epitaxial SiGe alloy layer to contract as they become equal to the lattice constant of the Si. The contraction in this case is the same in both the x and the y directions. On the other hand, the lattice constant of the epitaxial SiGe alloy layer in the growth direction (z) will expand to maintain a constant volume of the SiGe unit cell. Thus, strain is introduced in all three x, y, and z directions. As a result of the increase in lattice constant in the growth direction (z), the binding energy of the electrons along z will be decreased and the conduction band energy will be increased for the [001] and [00$\bar{1}$] carrier pockets (Δ_2 in Figure 3-7) relative to those of Si. Since the in-plane lattice constants of the SiGe alloy are similar to Si, the conduction band for the [100], [$\bar{1}$00], [010], and [0$\bar{1}$0] carrier pockets (Δ_4 in Figure 3-7) will have a similar energy with respect to those of Si. At the same time, this strain also lifts the degeneracy of the heavy hole (V_2 in Figure 3-7) and the light hole (V_1 in Figure 3-7) valence bands. The effect of this strain on the split-off valence band is much weaker. Figure 3-7 summarizes the strain effect on the electronic structure of an epitaxial layer of a SiGe alloy grown on a Si substrate with a growth direction of [001]. The energy for each band is referenced to the band structure of pure Si.

3.2 Assumptions and Approximations of the Si/SiGe Core-Shell Nanowire System

There is currently no data available for the effect of strain on the electronic structure of a SiGe alloy epitaxial layer grown on a Si wire. As a first start, the 2D result from Figure 3-7 will be used as a guide for the construction of a model for the core-shell nanowire consisting of a Si core and a SiGe alloy shell, with the wire direction taken along [001].

For simplicity, let us first approximate the wire cross section as a square and let us take the wire axis along [001] (labeled as the z axis). The growth of the SiGe epitaxial layer in this case will always be normal to the wire axis. Therefore, the maximum compression of the SiGe lattice constant will occur in the direction of the wire axis. In the directions normal to [001], two cases will be considered – the face normal to [100] (labeled as the x axis) and the face normal to [010] (labeled as the y axis). For the face normal to the x axis, the lattice of the epitaxial SiGe layer along the y and z axes are under compression, while the lattice along the x axis expands.

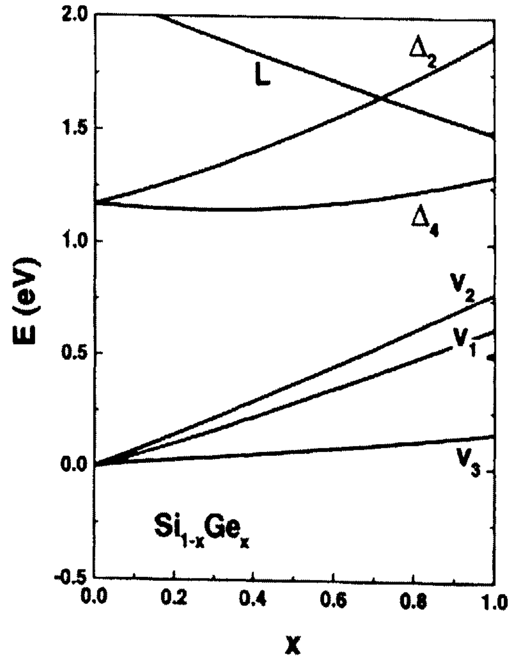

Figure 3-7: Energy of the conduction and valence band extrema for a strained $Si_{1-x}Ge_x$ alloy as a function of Ge concentration x for an epitaxial $Si_{1-x}Ge_x$ layer grown on a Si substrate with a growth direction of [001]. V_1, V_2, and V_3 denote the light-hole-like, heavy-hole-like, and split-off-like valence bands, respectively. Δ_2 denotes the conduction band with minima along [001] and $[00\bar{1}]$, whereas Δ_4 denotes the conduction band with minima along [100], $[\bar{1}00]$, [010], and $[0\bar{1}0]$. The conduction band minima at the L point of the strain $Si_{1-x}Ge_x$ layer relative to that of Si is denoted by L [5].

For the face normal to the y axis, the lattice of the epitaxial SiGe layer along the x and z axes contracts, whereas the lattice along the y axis expands. To summarize, the [001] direction is always under compression, while directions [100] and [010] will suffer a net expansion or compression, depending on the face under consideration.

When viewed in cylindrical coordinates for a cylindrical core-shell nanowire, the circumferential direction (which is a linear combination of the [100] and [010] directions) will experience a net contraction, but less than the contraction along the [001] direction. At the same time, the growth direction (which is also a linear combination of the [100] and [010] directions, but orthogonal to the circumferential direction) will experience a net expansion, with a magnitude depending on the number of layers that are grown. However, the expansion in this case is less than for the 2D case. Thus, the [100] and [010] directions (and their negative counterparts) experience a net expansion on average. As a first approximation, we consider the behavior along the [100] and [010] directions in the core-shell wire case to be similar to the behavior of the direction for the Δ_2 conduction pockets of the 2D case in Figure 3-7, while the behavior along the [001] direction is similar to the behavior of the direction of the Δ_4 conduction pockets for the 2D case in Figure 3-7. The approximation used here for modeling the cylindrical case is that the SiGe electron pockets with energy minima along the wire axis (denoted as Δ_{2c} in Figure 3-8) are assumed to have an energy deviation from Si that is similar to that of Δ_4 in Figure 3-7, while the energies for the other SiGe electron pockets with energy conduction band minima along the other two directions are assumed to be the same (denoted as Δ_{4c}) and are taken to have the x (Ge concentration) dependence of Δ_2 in Figure 3-7. The x dependence of the three valence bands is modeled to be the same as for the 2D case. In this way, a crude model for the band extrema for the core-shell nanowire is constructed. Figure 3-8 summarizes the band structure model assumed for the strained SiGe alloy layer for a Si/SiGe core-shell nanowire with a wire direction of [001].

In this thesis, the model calculation assumes a sharp interface between the Si core

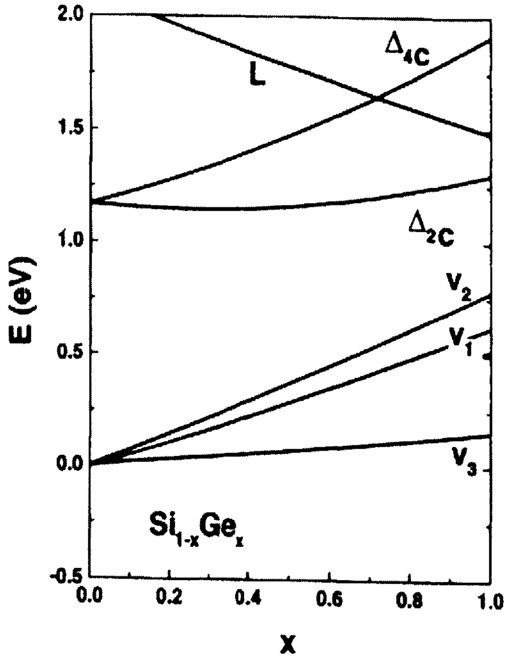

Figure 3-8: Energy of the conduction and valence band extrema as a function of x for a strained $Si_{1-x}Ge_x$ alloy epitaxial layer grown on a Si core wire with a wire direction of [001]. V_1, V_2, and V_3 denote light-hole-like, heavy-hole-like, and split-off-like valence bands, respectively. Δ_{2c} denotes the conduction band with minima along [001] and [$00\bar{1}$], Δ_{4c} denotes the conduction band with minima along [100] (corresponding to the nanowire axis), [$\bar{1}00$], [010], and [$0\bar{1}0$], and L denotes the conduction band with minima along <111>.

and the SiGe shell. The model neglects any grading concentration in the core or in the shell. The growth directions of both the Si core and the SiGe shell are assumed to be the same. The interface is modeled as a potential offset between the two materials. As a first approximation, the electron and hole effective masses of the SiGe alloy are taken either as the mass of Si or Ge, depending on the composition of the alloy (see Figure 3-4). This means that in the crudest approximation, we use the Si effective mass values for the Si-like band structure and the Ge effective mass values for the Ge-like band structure. This approximation can be improved if the mass components are known for Si and Ge at Δ and L, and we apply Vegard's law to obtain the mass components for the proper composition of the SiGe alloy. The core-shell nanowire is assumed to be imbedded in a non-conducting medium. The non-conducting medium is here modeled as a material with an infinite potential and thus there would only be transport in the wire direction.

3.3 Effect of Different Parameters on the Si/SiGe Core-Shell Nanowire System

The core-shell nanowire system depends on various parameters. The three parameters that have the greatest effect are the alloy composition of the SiGe alloy, the total core-shell wire diameter (e), the core wire diameter (d), and the shell thickness ($(e-d)/2$). These parameters determine the energy levels and quantum confinement effect of the system, which in turn govern the properties of the core-shell nanowire system.

From a thermoelectrics materials point of view, systems with a large quantum confinement effect are desired. It is the goal of this section to determine which configuration of the parameters in question will result in the best thermoelectric system.

Applying the model developed in Chapter 2 to the Si/SiGe core-shell nanowire system, the energy levels of this particular system are found. In the following subsections, the effect of different parameters on energy is presented only for the two lowest degenerate conduction bands (Δ_{2c}) and the highest valence band (V_2) in the strained SiGe shell material. To understand the role for the three parameters in determining the energy levels of the subbands, it is sufficient to consider only a few sample cases. From the analysis, one then can access the ranges of the parameters that are of interest for specific applications. The results obtained for the Δ_{2c} and the V_2 bands can then be used to generalize the effect of the three different parameters on the subband energies of the other conduction and valence bands in the strained SiGe layer (Δ_{4c} and V_1) and their possible occupation with carriers.

3.3.1 Effect of the Composition of the SiGe Alloy Layer

A different SiGe shell composition results in different band offsets (V_{cond} and -V_{val}) at the interface between the core and the shell layer. V_{cond} and -V_{val} are each taken to be the energy difference between the band extrema for the shell SiGe alloy with respect to that for the core Si conduction and valence bands, respectively. Figure 3-8 shows that over the whole range of x (Ge concentration), the conduction band offset V_{cond} of the Δ_{2c} band varies from -0.1 eV to 0.1 eV, whereas the valence band offset -V_{val} of the V_2 band ranges from 0 eV to 0.8 eV.

A schematic view of the electron's energy levels of the core-shell nanowire system for the first case of $V_{cond} > 0$ for Δ_{2c} with -$V_{val} > 0$ for V_2, and for the second case of $V_{cond} < 0$ for Δ_{2c} with -$V_{val} > 0$ for V_2 are shown in Figure 3-9 (a) and (b), respectively.

Conduction Band

Since the lowest SiGe conduction bands (Δ_{2c}) result in both positive and negative potential offsets at the interface, the distribution of the probability density of electrons changes with the composition of the SiGe alloy layer. For example, when the strained SiGe shell results in a positive conduction band offset at the interface ($V_{cond} > 0$),

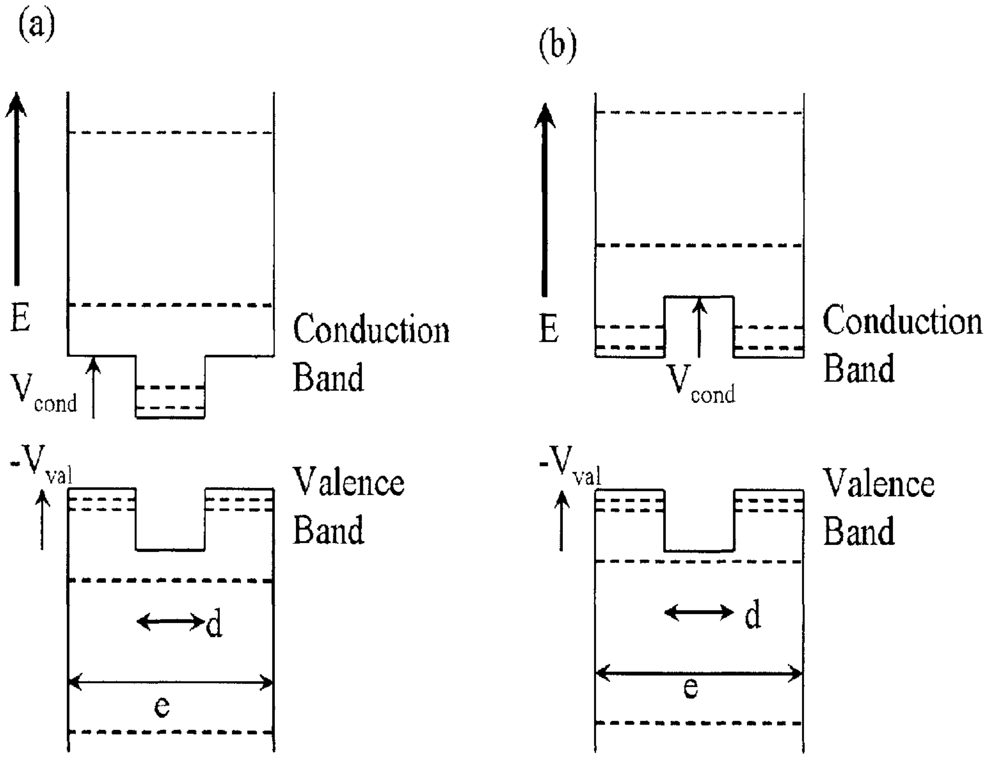

Figure 3-9: Schematic view of the energy levels for the core-shell nanowire system for the case of (a)V_{cond} >0 for Δ_{2c} with -V_{val} >0 for V_2, and (b)V_{cond} <0 for Δ_{2c} with -V_{val} >0 for V_2. This figure is NOT drawn to scale.

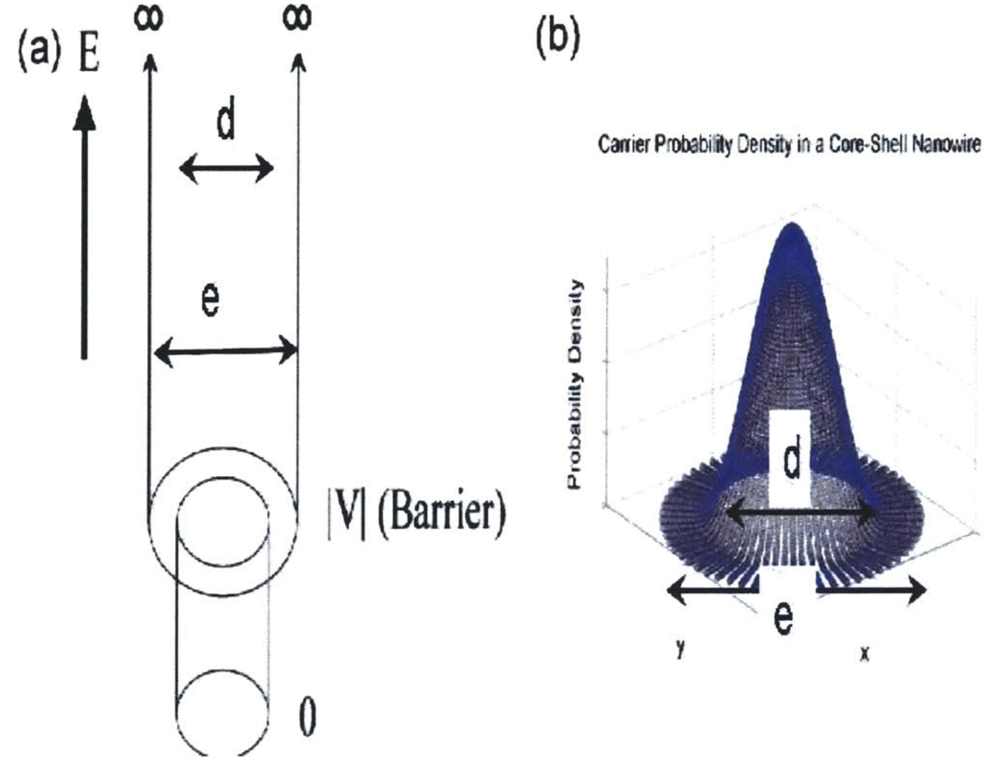

Figure 3-10: (a) Energy diagram and (b) carrier probability density distribution of the lowest electron energy eigenstate of the general case, where the Si core acts as the potential well for the Si/SiGe core-shell nanowire. x and y denote the real space axes for the core-shell nanowire.

the core Si acts as an electron potential well (see Figure 3-10(a)). This leads to a higher probability of finding electrons in the Si core than in the SiGe alloy shell. For illustration, Figure 3-10(b) shows the probability distribution of the lowest energy electron eigenstate, indicating that the electrons are highly localized in the Si core region.

On the other hand, if the SiGe alloy layer results in a negative conduction band offset at the interface (V_{cond} <0), the Si core becomes a potential barrier (see Figure 3-11(a)). This results in a higher probability of finding the electrons in the alloy shell. Figure 3-11(b) shows the probability distribution of the electrons in the lowest energy eigenstate as an illustration. Thus, as the composition changes (as V_{cond}

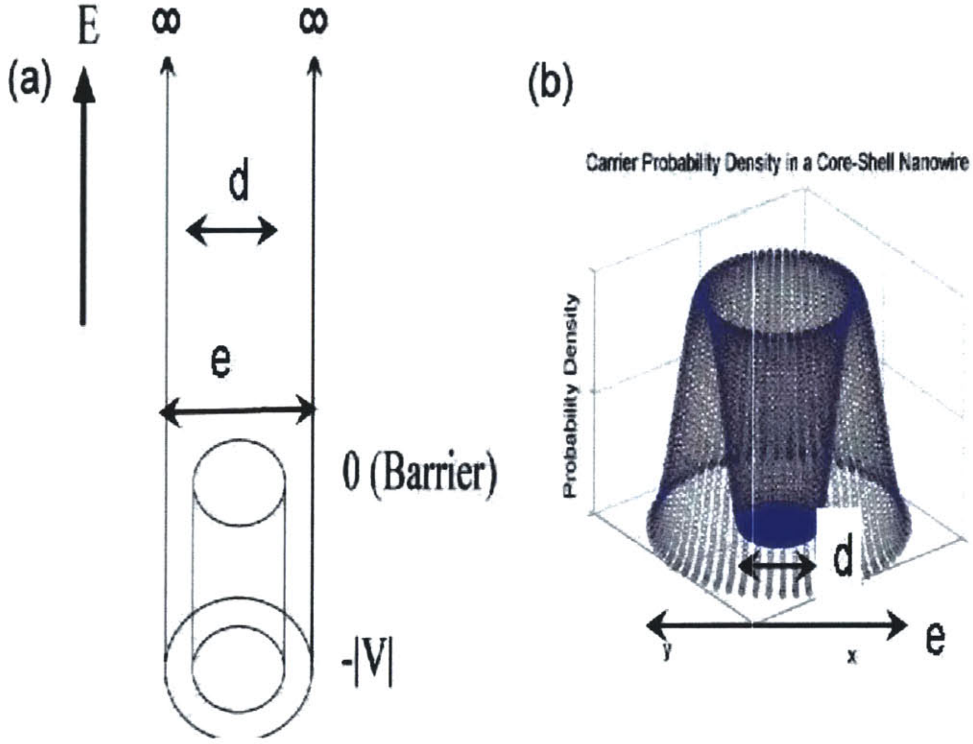

Figure 3-11: (a) Energy diagram and (b) carrier probability density distribution of the lowest electron energy eigenstate of the general case, where the Si core acts as the potential barrier for the Si/SiGe core-shell nanowire. x and y denote the real space axes for the core-shell nanowire.

correspondingly changes), the electron probability density changes between being the highest in the shell for V_{cond} <0 to being the highest in the core for V_{cond} >0.

The magnitude of the interface conduction band offset (V_{cond}) plays a major role in the determination of: (1) the number of energy levels being confined in the lower potential region and (2) where the lowest subband level lies. Since the chemical composition in the SiGe shell layer determines the magnitude of the offset at the interface, as shown in Figure 3-8, any change in composition changes the number of energy levels being confined in the lower potential region. The V_{cond} effect on the number of energy levels that are confined is now illustrated for 3 different cases.

Figure 3-12(a) shows the V_{cond} effects on the first 20 conduction energy levels for the case of large e and $d \approx e$ (thin shell). In this case, as V_{cond} goes from negative to positive, the number of conduction energy levels that are confined goes from 0 to a large number. Figure 3-12(b) shows the V_{cond} effects on the first 20 energy levels for the case of a large e with $d << e$ (thick shell). In this case, as V_{cond} goes from negative to positive, the number of conduction energy levels that are confined goes from a large number to close to 0. As can be seen from Figure 3-12 (especially the lowest energy level in Figure 3-12(b)), the choice of d also has a large effect on the number of energy levels being confined and on the energy of the levels. The effect of d will be discussed in detail in Section 3.3.3.

Figure 3-13 illustrates the V_{cond} effect on the first 20 energy levels for the case of small e and $d \approx e$ (small core and thin shell). This case might not be realistic from a fabrication standpoint. However, it shows that the conduction band energy levels depend not only on V_{cond}, but also on the parameters d and e. In this case, as V_{cond} goes from negative to positive, the number of conduction subband energy levels that are confined is unchanged. Comparing Figure 3-12(b) with Figure 3-13, one can see that e also plays a role in determining the number of energy levels being confined, as well as the energy of the levels. The effect of e will be discussed in detail in Section 3.3.2.

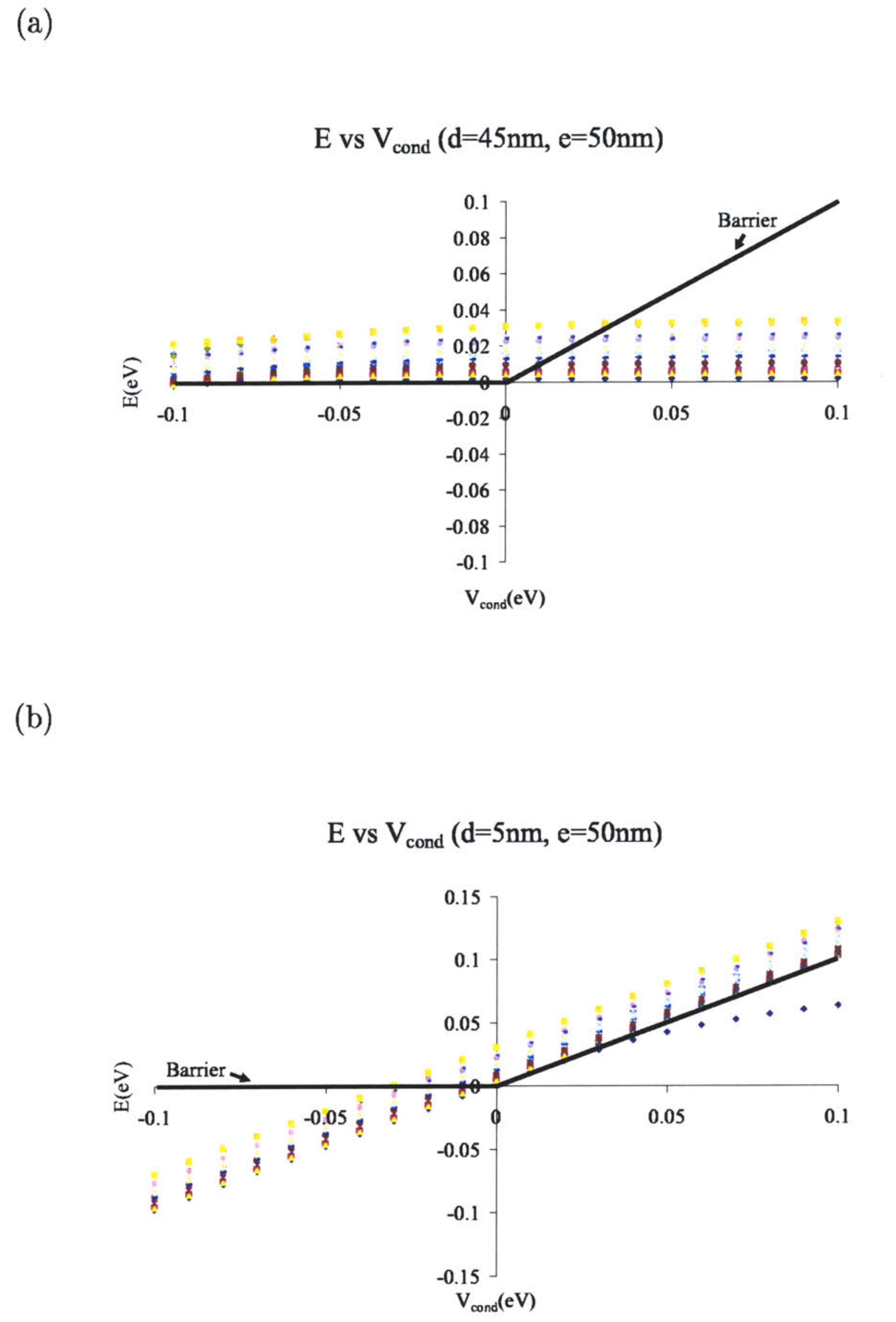

Figure 3-12: Effect of the potential offset at the interface on the first 20 subband conduction levels of the core-shell nanowire system for (a)d=45nm with e=50nm, and (b)d=5nm with e=50nm.

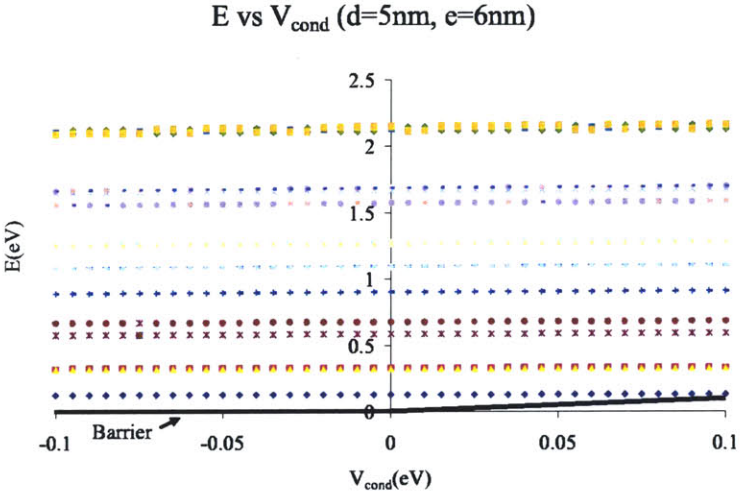

Figure 3-13: Effect of the potential offset V_{cond} at the core-shell interface on the first 20 subband conduction levels of the core-shell nanowire system for d=5nm with e=6nm (small core and thin shell).

Valence Band

For the valence band, changing the composition of the SiGe alloy results in only a positive shift in electron energy at the interface (see Figure 3-8). This shift is equivalent of a negative shift in hole energy at the interface. Thus, the Si core always acts like a hole barrier for all ranges of Ge composition x (see Figure 3-11). As a result, any changes in the shell composition only lead to the change of the magnitude of the band offset between the interface, which affects the amplitude of the probability density and number of valence energy levels being confined in the shell. The effect of V_{val} on the energy levels is shown in Figure 3-14 and Figure 3-15 for the same cases considered in the last section for the cases of the conduction band.

From Figure 3-14 and Figure 3-15, one can see a similar effect of V_{val} on the number of valence subbands being confined as for the conduction subband case (see Figure 3-12 and Figure 3-13). The only difference in the valence band case is that V_{val} is always negative and can be as negative as -0.8 eV. When V_{val} gets this negative, almost all of the valence subbands will have very negative energies, resulting in a large hole confinement in the shell region of the core-shell structure.

Summary

Looking at the variation of the band offset energies alone, one can conclude that systems with small e and a relative small magnitude of the band offset result in a much larger quantum effect than systems with large e. Thus, one should expect that in order for the core-shell nanowire system to result in good thermoelectrics performance, a small e and some small offset ($\sim k_BT \approx 26\,\text{meV}$ at T=300 K) are desired.

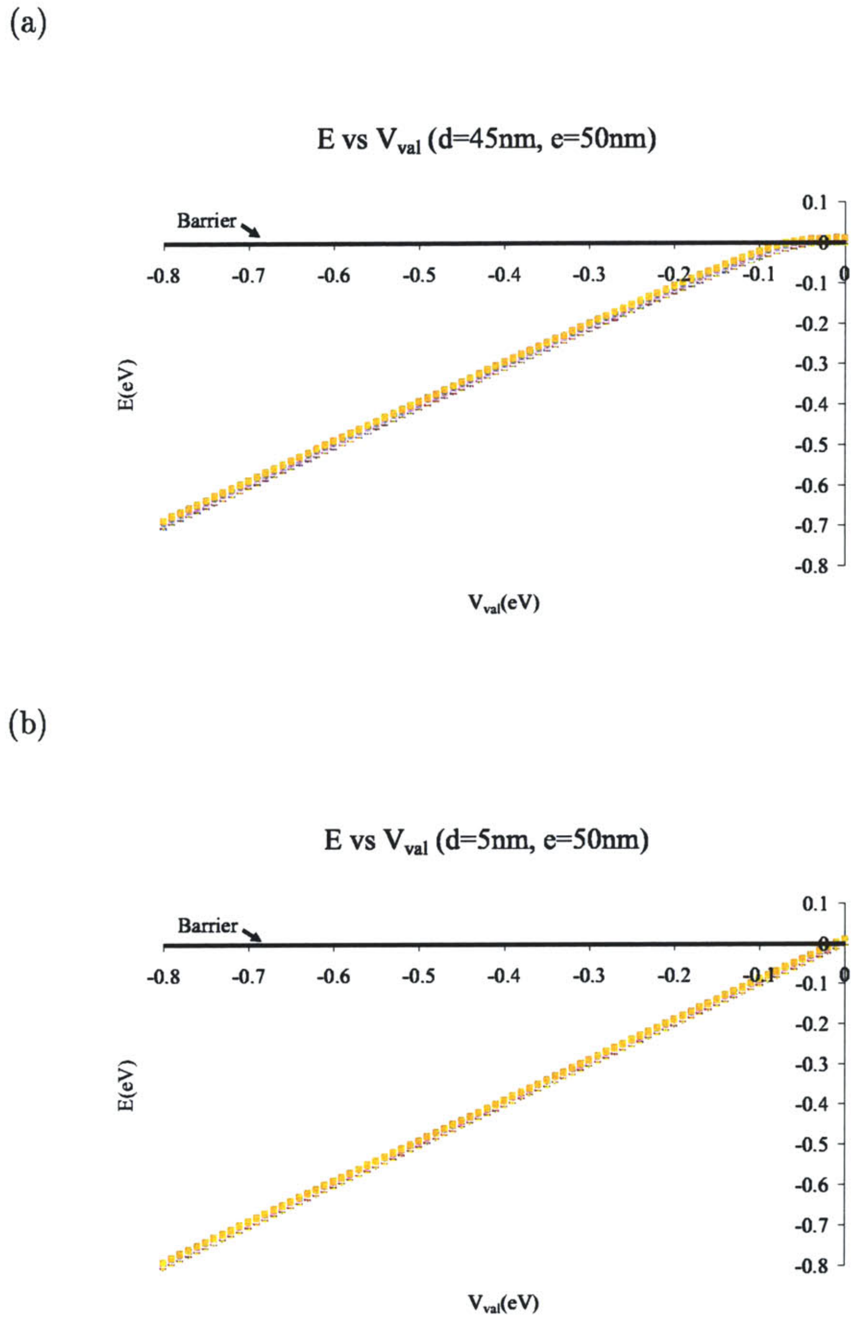

Figure 3-14: Effect of the potential offset V_{val} at the core-shell interface on the first 20 subband valence levels of the core-shell nanowire system for (a)d=45nm with e=50nm (thin shell), and (b)d=5nm with e=50nm (thick shell).

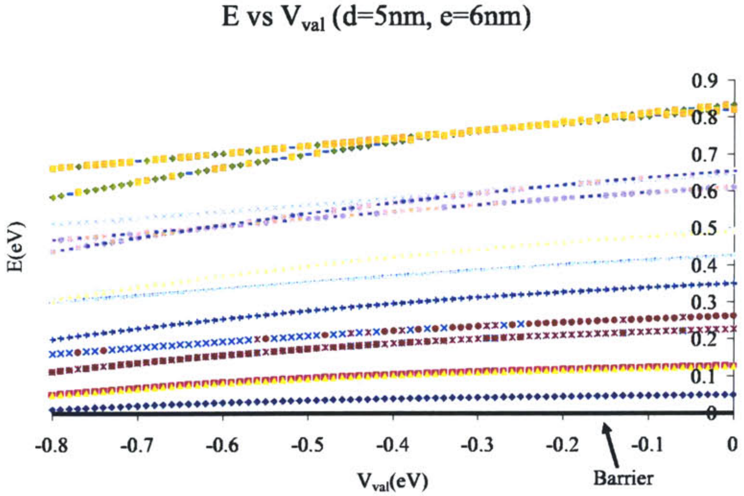

Figure 3-15: Effect of the potential offset V_{val} at the core-shell interface on the first 20 subband valence levels of the core-shell nanowire system for d=5nm with e=6nm.

3.3.2 Effect of the Total Core-Shell Diameter (e)

The total core-shell diameter (e) plays a major role in the determination of the subband energies and the subband energy separation of the core-shell nanowire system. The quantum confinement effect of the system only occurs when the total core-shell diameter is small. The effects of the core diameter and of the shell thickness are secondary effects relative to the total core-shell diameter. For example, at a large total core-shell diameter, there is very little quantum confinement effect, and the separation between the energy levels is small compared to k_BT (26 meV at T=300 K). As the total core-shell diameter gets smaller, the separation between the subband energies of the system becomes larger and the overall energy of each subband increases. At a very small total core-shell diameter, the effect of the quantum confinement becomes so large that the system acts as if the potential barrier of the interface does not exist. Figure 3-16 and Figure 3-17 illustrate the effect of the total core-shell diameter (e)

for different constant core diameter values and for different interface offset energies (V_{cond}) on the conduction subband levels, while Figure 3-18 illustrates the effect of the total core-shell diameter for different constant core diameter values and for different interface offset energies (V_{val}) on the valence subband levels.

As seen from Figure 3-16, Figure 3-17, and Figure 3-18, the energies of all the subband levels are identical in most cases at small e values, and the energy separations between the subband levels are identical for all cases at small e values. Thus, e has the most influence on the energies of the subband levels and on the energy separations between the subbands. At the same time, d, V_{cond}, and V_{val} also have a small influence on the energies of the subbands, resulting in a difference in the barrier cross-over point for these figures. However, d, V_{cond}, and V_{val} have no influence on the separation of the energy levels. The effect of d will be discussed in detail in Section 3.3.3, whereas the effect of V_{cond} and V_{val} has already been discussed in detailed in Section 3.3.1.

One can look at the total core-shell diameter as the length that determines the quantum confinement requirement for the system, whereas the confinement effect of the core diameter or of the shell thickness is in part contained within the effect of the total core-shell diameter.

Summary

The results of this subsection alone suggest that the quantum confinement effects only occur for small values of e. Once again, good thermoelectric performance points to using a core-shell nanowire with small e values.

3.3.3 Effect of the Si Core Diameter (d) and of the SiGe Shell Thickness ($(e-d)/2$)

The effect of the core diameter can be seen in two different situations: the core as a potential well or the core as a potential barrier. The effect of varying the shell

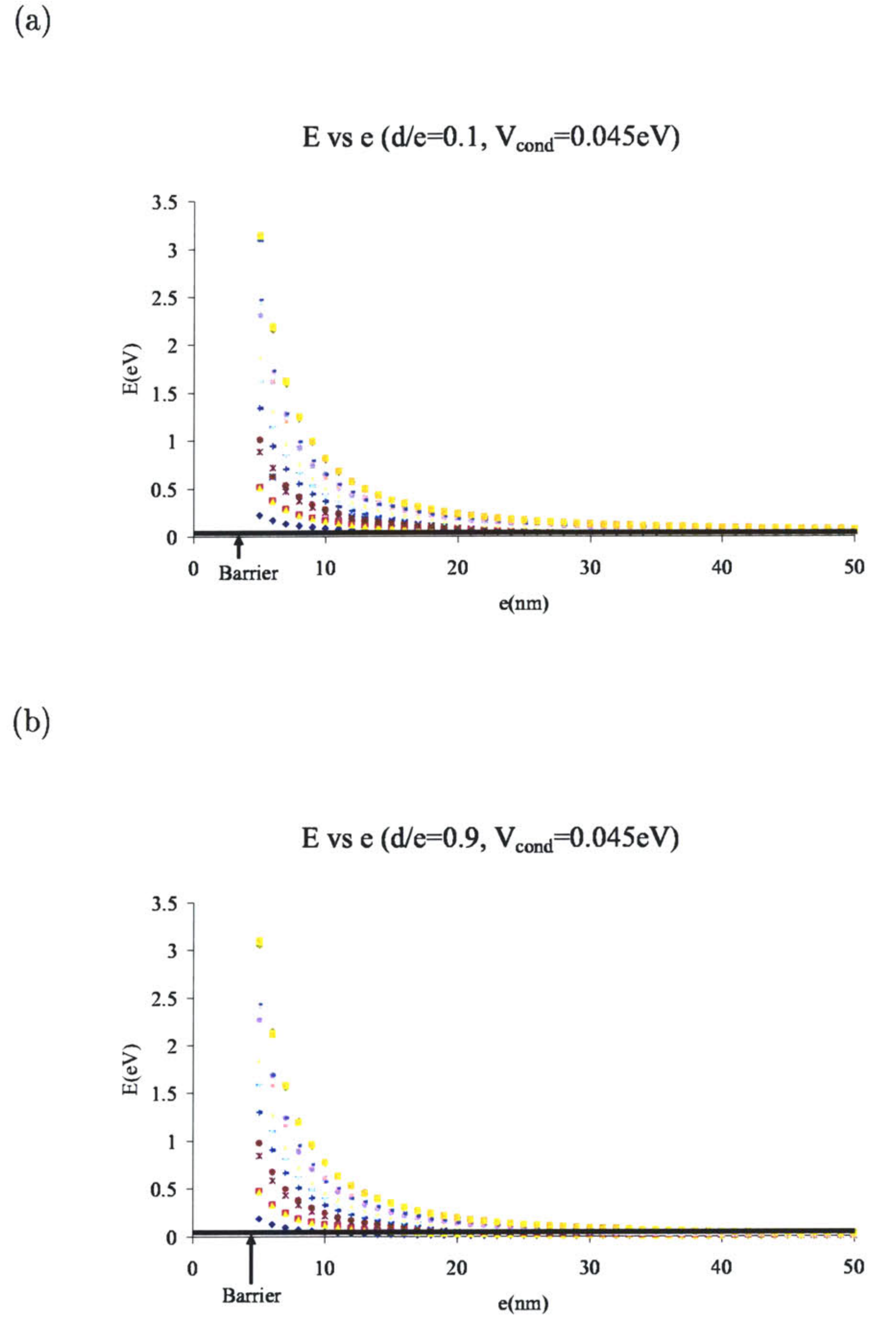

Figure 3-16: Effect of the total core-shell diameter on the first 20 subband conduction levels of the core-shell nanowire system for (a)d/e=0.1 with V_{cond}=0.045eV, and (b)d/e=0.9 with V_{cond}=0.045eV.

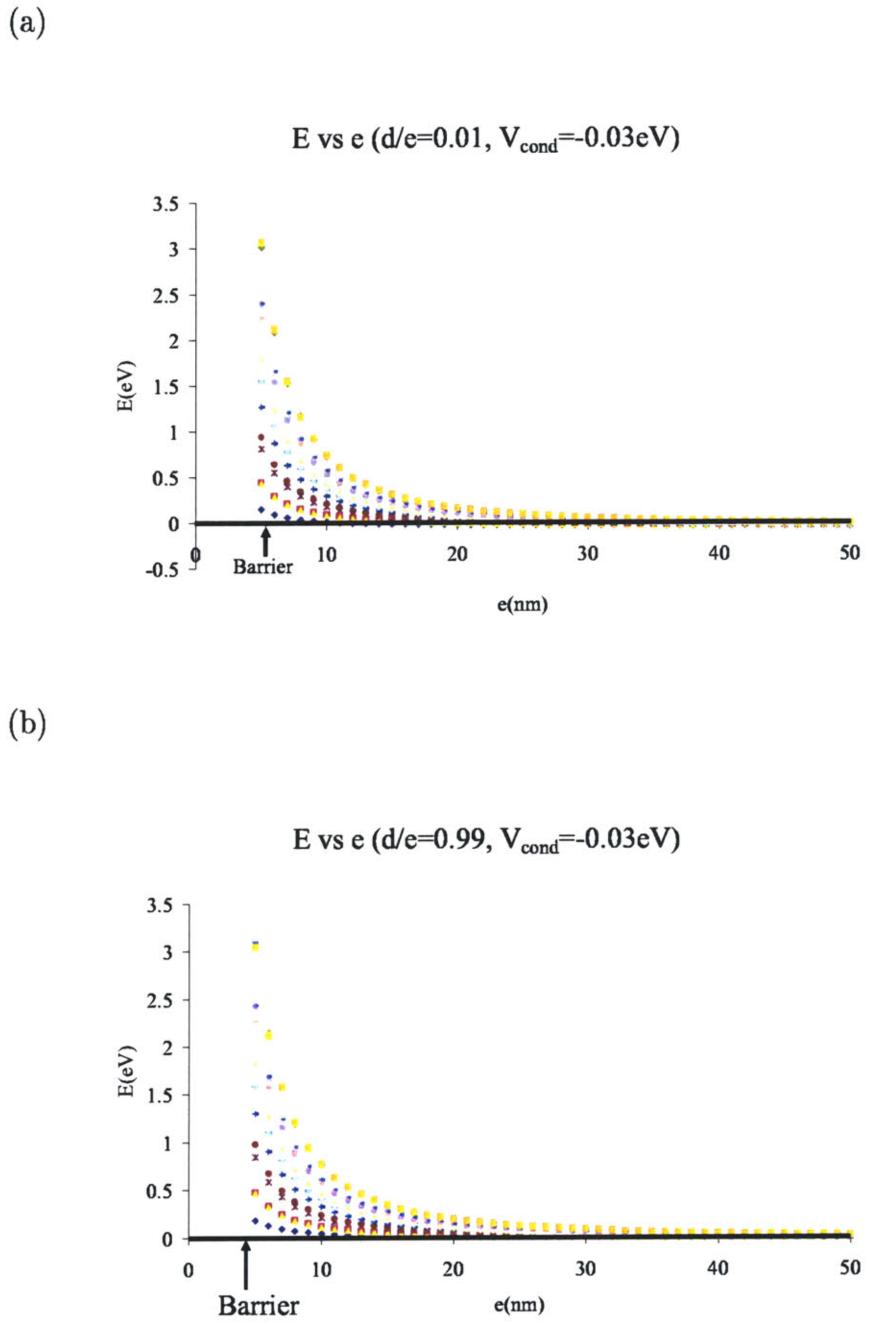

Figure 3-17: Effect of the total core-shell diameter on the first 20 subband conduction levels of the core-shell nanowire system for (a)d/e=0.01 with V_{cond}=-0.03eV, and (b)d/e=0.99 with V_{cond}=-0.03eV.

(a)

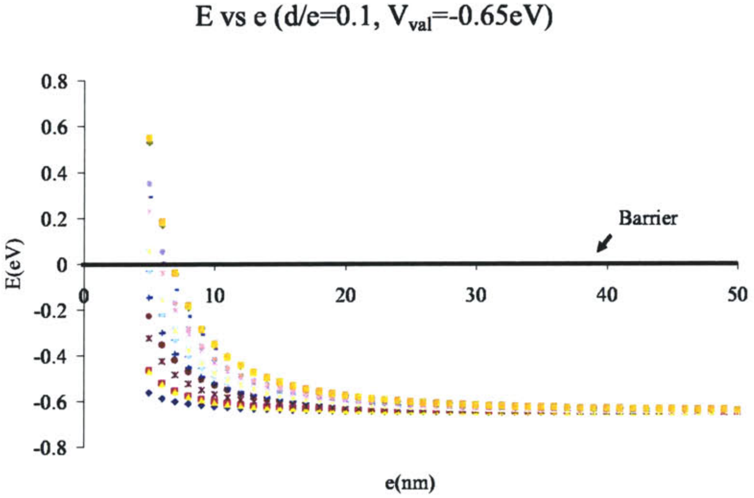

(b)

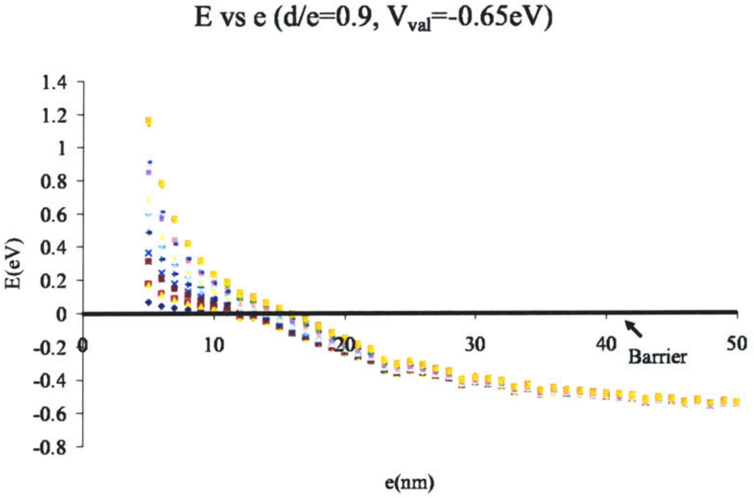

Figure 3-18: Effect of the total core-shell diameter on the first 20 subband valence levels of the core-shell nanowire system for (a)d/e=0.1 with V_{val}=-0.65eV, and (b)d/e=0.9 with V_{val}=-0.65eV.

thickness $((e-d)/2)$ is simply the opposite of the effect of varying the core diameter (d) at constant e.

The Core as a Potential Well

When the core acts as a potential well, it has a lower energy than the shell and tries to trap carriers in the core (see Figure 3-10). At a very small core diameter, there is a large quantum confinement effect within the core, but very little in the shell. Thus, this effect results in an energy increase of the subbands that would have been trapped in the core. As a result, all of the subbands will have energies above the potential barrier introduced at the interface. As the core diameter increases, the quantum confinement effect within the core decreases and the energy of the system starts to decrease. As the core diameter approaches the core-shell diameter, the effect of the quantum confinement in the core will diminish and this results in carrier trapping in the core. Figure 3-19 summarizes the effect of core diameter for the conduction bands of a core-shell nanowire where the core acts as a potential well for the case of a small e and of a large e. The difference in the behavior of the two cases in Figure 3-19 is due to the effect of e (see Section 3.3.2).

The Core as a Potential Barrier

The effect is reversed when the core acts as a potential barrier. At small core diameter values, the shell thickness is large and the quantum confinement effect is small in the shell, resulting in carrier trapping in the shell. As the core diameter increases, the shell thickness decreases, resulting in a larger quantum confinement effect in the shell. As the core approaches the core-shell diameter, the quantum confinement effect in the shell is so large that there is little trapping occurring in the shell. Figure 3-20 and Figure 3-21 summarize the effect of the core diameter on the conduction subband levels and the valence subband levels, respectively. Once again, the difference in the behavior within each figure is due to the effect of e (see Section 3.3.2).

(a)

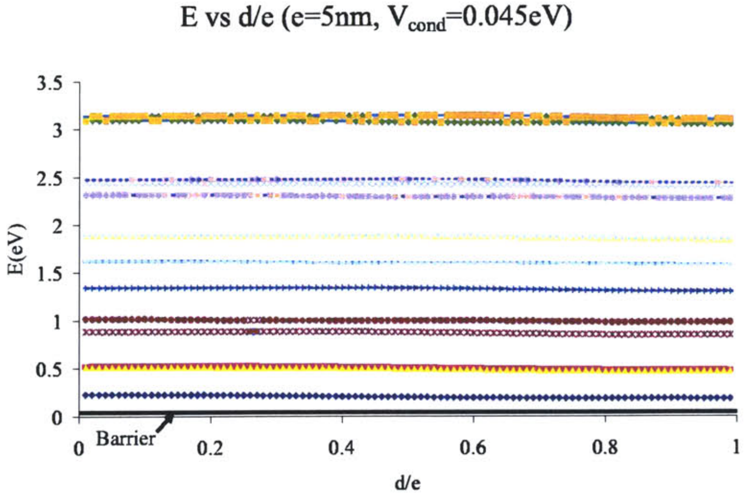

(b)

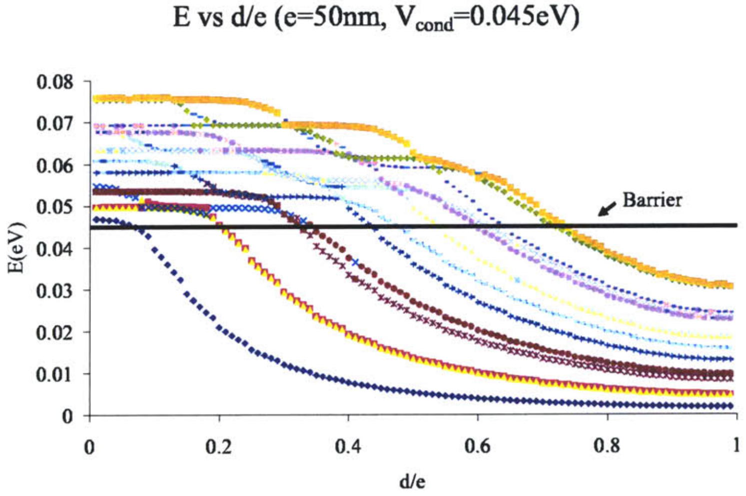

Figure 3-19: Effect of the core diameter on the first 20 subband conduction levels of the core-shell nanowire system for (a)e=5nm with V_{cond}=0.045eV, and (b)e=50nm with V_{cond}=0.045eV.

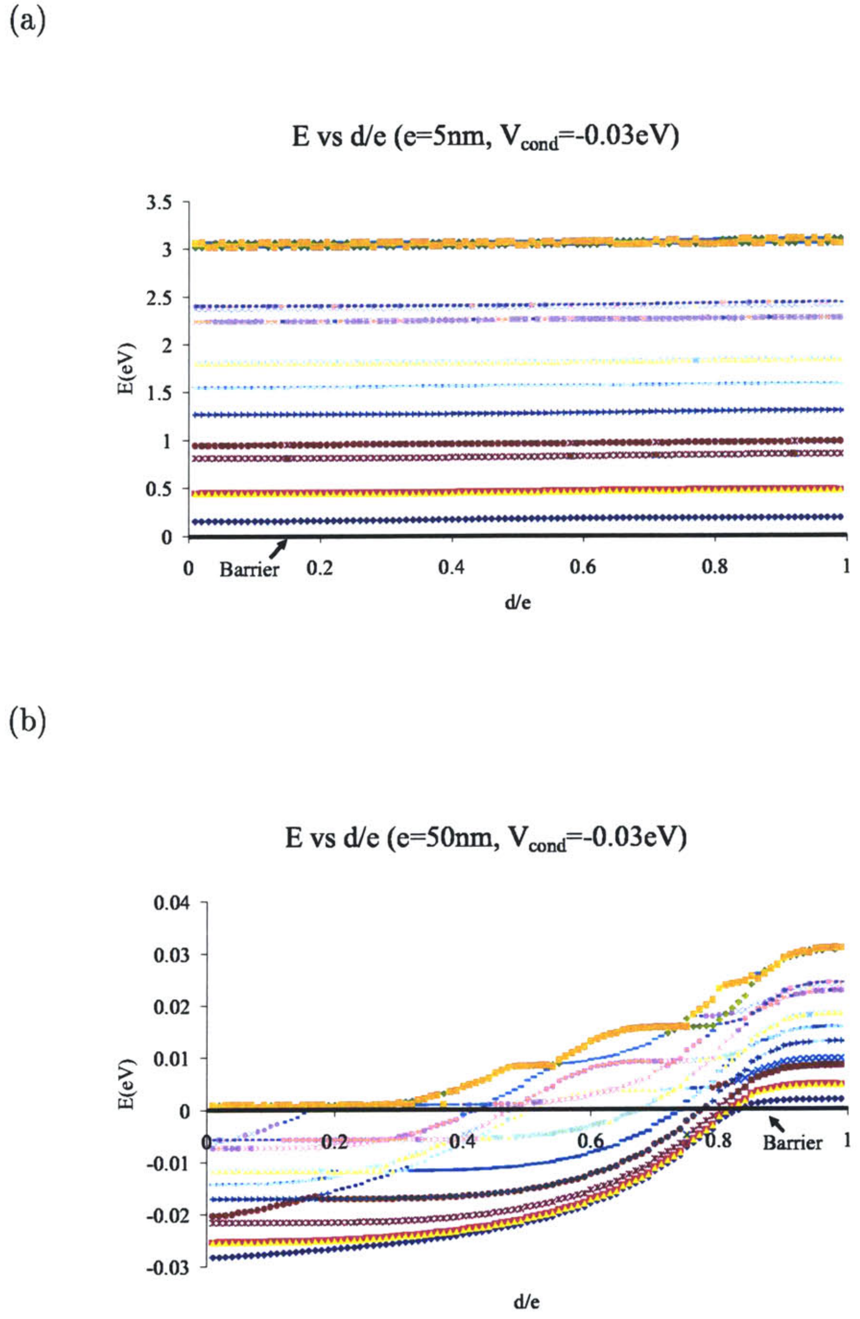

Figure 3-20: Effect of the core diameter on the first 20 subband conduction levels of the core-shell nanowire system for (a)e=5nm with V_{cond}=-0.03eV, and (b)e=50nm with V_{cond}=-0.03eV.

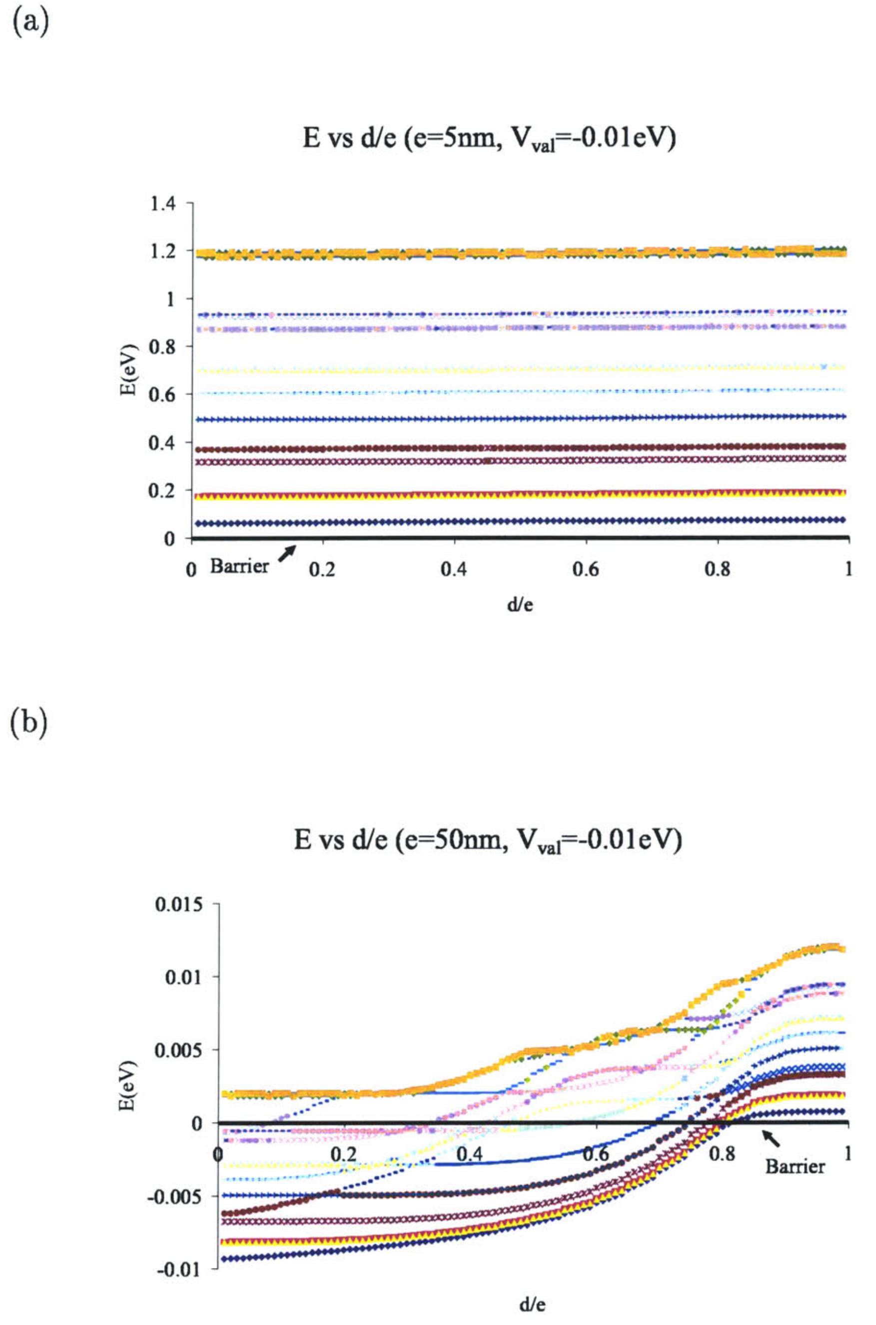

Figure 3-21: Effect of the core diameter on the first 20 subband valence levels of the core-shell nanowire system for (a)e=5nm with V_{val}=-0.01eV, and (b)e=50nm with V_{val}=-0.01eV.

Summary

From the results of this subsection, it is found that a proper choice of d is also very important for the core-shell nanowire system to have a large quantum mechanical effect. Thus, depending on whether the core acts like a well or a barrier for the carriers, one should choose d so that only a small trapping or no trapping effect results. For example, $d << e$ is desirable for the case of V_{cond} >0, whereas, $d \approx e$ is desirable for the case of V_{cond} <0 or V_{val} <0.

3.3.4 Conclusions

As seen from Section 3.3.1, Section 3.3.2, and Section 3.3.3, both d, e, and V have a huge effect on the determination of the actual energies of the conduction subband levels and of the valence subband levels. The separation between the subband levels is mostly controlled by e. For the case where the core acts like a potential well ($V_{cond} > 0$), e has the largest effect on the determination of the energy separation and on the energy of the subband levels. Having fixed the value of e, d plays the role of determining the number of subband levels that are inside the core potential well. As for the core as potential barrier case ($V_{cond} < 0$ and $V_{val} < 0$), the role of e is similar to that for the $V_{cond} > 0$ case. However, the effect of d is reversed for the cases of $V_{cond} < 0$ and $V_{val} < 0$ relative to the cases of $V_{cond} > 0$. Namely, for the $V_{cond} < 0$ and $V_{val} < 0$ cases, d plays the role of determining the number of subband levels that are inside the shell potential well for a fixed e.

After performing the analysis in this section, we come to the conclusion that the core-shell nanowire system with the greatest quantum mechanical effect is the one with a small e, a relatively small magnitude of the offset V (resulting in only few or no subband levels being confined), and a d that results in a secondary confinement effect in the lower potential energy region (in the core for the case of $V_{cond} > 0$ and in the shell for the case of $V_{cond} < 0$ or $V_{val} < 0$). Thus, the core-shell nanowire system with these ranges for the 3 parameters controlling the geometric and energy configurations is expected to have the greatest potential for showing good thermoelectric performance.

Chapter 4

Transport Properties of the Doped Si/SiGe Core-Shell Nanowires

A semi-classical model is applied in this chapter to derive various transport properties of the core-shell nanowire system. Section 4.1 gives a brief summary of a semi-classical model for a nanowire. Approximations and assumptions used for the calculation of the core-shell nanowire are discussed in Section 4.2. The transport results of the core-shell nanowire system are summarized in Section 4.3. The chapter concludes with consideration of the effect of different parameters on ZT in Section 4.4.

4.1 Semi-Classical Transport Model

Recalling from Chapter 1, the thermoelectric performance of a materials system depends on its dimensionless thermoelectric figure of merit (ZT). According to $ZT = S^2\sigma T/(\kappa_e + \kappa_L)$, ZT depends on the electrical conductivity (σ), the Seebeck coefficient (S), the electrical thermal conductivity (κ_e), the lattice thermal conductivity (κ_L), and the temperature (T). In Section 4.1.1, the treatment of the terms σ, S, and κ_e are considered, while in Section 4.1.2, the treatment of κ_L is considered.

4.1.1 Electrons

The semi-classical model is used to derive various transport coefficients (σ, S, and κ_e) for the core-shell nanowire system. The semi-classical model is based on the Boltzmann transport equation. The Boltzmann transport equation has been studied for 1D, 2D, and 3D systems [16, 7, 8, 17]. For a simple one-band model in β dimensions, the carrier density (n), the electrical conductivity (σ), the Seebeck coefficient (S), and the electrical thermal conductivity (κ_e) are derived as [16, 7, 8]:

$$\begin{aligned} n_\beta &= \int 2\frac{\overrightarrow{dk}}{(2\pi)^\beta} f(E), && (4.1)\\ \sigma &= L_\beta^{(0)}, && (4.2)\\ S &= -\frac{1}{eT}\frac{L_\beta^{(1)}}{L_\beta^{(0)}}, && (4.3)\\ \kappa_e &= \frac{1}{e^2T}(L_\beta^{(2)} - \frac{(L_\beta^{(1)})^2}{L_\beta^{(0)}}), && (4.4) \end{aligned}$$

where T is the temperature in degrees Kelvin, and

$$L_\beta^{(\alpha)} = 2e^2 \int \frac{\overrightarrow{dk}}{(2\pi)^\beta}\left(-\frac{df}{dE}\right)\tau(E(k))v(k)v(k)(E(k) - E_f)^\alpha, \qquad (4.5)$$

where the factor of 2 accounts for the electron spin, β is the dimension of the system under consideration, $\alpha = 0, 1, 2$, while $\overrightarrow{dk}$ is the differential element in β dimensional k space, $E(k)$ denotes the carrier dispersion relation, $\tau(E(k))$ is the relaxation time which in general depends on $E(k)$, E_f is the Fermi energy, and $f(E)$ is the Fermi-Dirac distribution function,

$$f(E) = \frac{1}{1 + e^{(E-E_f)/(k_BT)}}. \qquad (4.6)$$

In order to compare the 1D coefficients with the bulk coefficients, the 1D coefficients that are sensitive to dimensionality, namely n_β and $L_\beta^{(\alpha)}$, are divided by an extra cross sectional area term. The cross sectional area for a nanowire with radius $(d_w)/2$ is $\pi(d_w)^2/4$. The 1D $L_{1D}^{(\alpha)}$ and n_{1D} then become

$$L_{1D}^{(\alpha)} = 4e^2 \int \frac{\overrightarrow{dk}_{1D}}{(\pi d_w)^2} \left(-\frac{df}{dE}\right) \tau(E(k))v(k)v(k)(E(k) - E_f)^\alpha, \tag{4.7}$$

$$n_{1D} = \int \frac{4\overrightarrow{dk}_{1D}}{(\pi d_w)^2} f(E) = \int g(E)f(E)dE, \tag{4.8}$$

where $g(E)$ denotes the electronic density of states and $\overrightarrow{dk}_{1D}$ is the differential element in 1D k space. The calculation of Equation (4.5) or Equation (4.7) requires knowledge of the relaxation time $\tau(E(k))$. In general, consideration of detailed relaxation processes and their energy dependence is a rather difficult task for the computation of $\tau(E(k))$. For simplicity, an approximation known as the constant relaxation time approximation (RTA) has been employed for the formulation of general model calculations, leaving the consideration of specific scattering mechanisms and their energy dependence to more accurate and systematic detailed studies of specific materials systems [18, 19].

In the constant RTA model, $\tau(E(k)) = \tau$ is considered to be constant in both E and k space. The relaxation time τ can then be simply related to the carrier mobility μ along the wire by

$$\tau = \frac{\mu m^*}{e}, \tag{4.9}$$

where m^* and μ are the transport effective mass and mobility along the wire direction, respectively. With the constant RTA approach, the integration of Equation (4.5) and Equation (4.7) can be carried out readily given the dispersion relation $E(k)$.

In any systems, there are many energy bands that need to be taken into consideration due to the degeneracy of the multiple carrier pockets at the conduction band and valence band extrema. For a quantum wire system, besides the degeneracy effect, quantum confinement also introduces band splitting, and results in a set of subbands that comes from a single band of the bulk material. Therefore, when considering the transport properties of a 1D system, contributions from all of the subbands with band extrema close to the Fermi energy (within $\sim 10k_BT$) need to be included. For a multi-band system, the n and $L^{(\alpha)}$'s in Equations (4.1)–(4.4) needs to be replaced by the sum $n_{total} = \sum_j n_j$ and $L^{(\alpha)}_{total} = \sum_j L^{(\alpha)}_j$ of contributions from each subband j, and the quantities n, σ, S, and κ_e become

$$\begin{aligned} n_{total} &= \sum_j n_j, & (4.10)\\ \sigma_{total} &= \sum_j L^{(0)}_j, & (4.11)\\ S_{total} &= -\frac{1}{eT}\frac{\sum_j L^{(1)}_j}{\sum_j L^{(0)}_j}, & (4.12)\\ \kappa_{e,total} &= \frac{1}{e^2T}\Big(\sum_j L^{(2)}_j - \frac{(\sum_j L^{(1)}_j)^2}{\sum_j L^{(0)}_j}\Big), & (4.13) \end{aligned}$$

4.1.2 Phonons

Besides n, σ, S, and κ_e, the lattice thermal conductivity (κ_L) is another quantity of interest for thermoelectric applications. κ_L and κ_e together sum to be the total thermal conductivity $\kappa = \kappa_e + \kappa_L$ of the system. From kinetic theory, the thermal conductivity of a single branch phonon is given by [20]

$$\kappa_L = \frac{1}{3}C_v v_s l_p, \tag{4.14}$$

where C_v is the heat capacity per unit volume, v_s is the sound velocity of the phonon in that branch, and l_p is the phonon mean free path.

The bulk single branch phonon mean free path can be calculated according to Equation (4.14), given the values of C_v, v_s, and κ_L for that branch. For a system with multiple phonon branches, $\kappa_{L,total}$ becomes the sum of $\kappa_{L,j}$ where j is the index for each phonon branch, namely,

$$\kappa_{L,total} = \sum_j \kappa_{L,j} = \frac{1}{3} \sum_j C_{v,j} v_{s,j} l_{p,j}. \tag{4.15}$$

However, the measured values of C_v and κ_L given in the literature already account for contributions from all of the phonon branches. For a rough approximation, an effective v_s can be estimated as a weighted sum of $v_{s,j}$ over all branches as follows [21],

$$v_s^{-3} = 3(v_L^{-3} + 2v_T^{-3}), \tag{4.16}$$

where v_L and v_T denote the velocity of sound for the longitudinal acoustic phonon branch and the transverse acoustic phonon branches, respectively. Using the measured values of C_v and κ_L with Equation (4.16), l_p can then be calculated.

For a nanowire system, the electrons are well confined within the wire, but not the phonons. Rather, the nanowire interface acts like a scattering center for the phonons. When the phonons reach the interface, they are scattered, resulting in a decrease in lattice thermal conductivity. As the diameter of the nanowire decreases, the lattice thermal conductivity decreases due to the increase in the phonon interface scattering. This phenomenon results in a decrease in the phonon mean free path. As a first approach, the phonon mean free path (l_p) could be modeled as a weighted average of the bulk phonon mean free path ($l_{p,bulk}$) and the nanowire diameter (d_w) as follows,

$$\frac{1}{l_p} = \frac{1}{l_{p,bulk}} + \frac{1}{d_w}. \tag{4.17}$$

Thus, as the nanowire diameter decreases to a length much smaller than the bulk phonon mean free path, a dramatic decrease in the lattice thermal conductivity is expected. This decrease in thermal conductivity is one of the reasons why enhancement in thermoelectric performance results from low dimensional systems.

4.2 Assumptions and Approximations for the Core-Shell Nanowire System

4.2.1 Electrons

For the core-shell nanowire model under consideration, the electrons are considered to be well confined within the wire and there is only transport along the wire direction. As seen from Chapter 3, the electrons can be further confined to the core region or to the shell region, depending on the interface conduction band extrema and valence band extrema offset. However, this type of confinement only applies to the electrons in the lowest energy levels. Moreover, there is still some probability for these low energy electrons to be in the non-confined region of the core-shell structure. Therefore, for simplicity, the electrons are assumed to travel throughout the entire core-shell nanowire with a probability determined by the results of Chapter 3. Thus, the d_w in Equation (4.7) and Equation (4.8) will be replaced by the total core-shell diameter (e). Furthermore, the mobility of the electrons is taken to be the lowest intrinsic mobility of the two materials. These two approximations together form a crude approximation for treating the electrons. These approximations for the electrons represent the worst case scenario for the values of the coefficients appearing in the transport equations. Thus, if the results are promising, there is much confidence that the device will have a promising thermoelectric performance.

4.2.2 Phonons

The lattice thermal conductivity (κ_L) is found by considering the thermal current between two points of a material (Q), which is given by [22]

$$Q = \kappa_L A(-\frac{\partial T}{\partial x}), \tag{4.18}$$

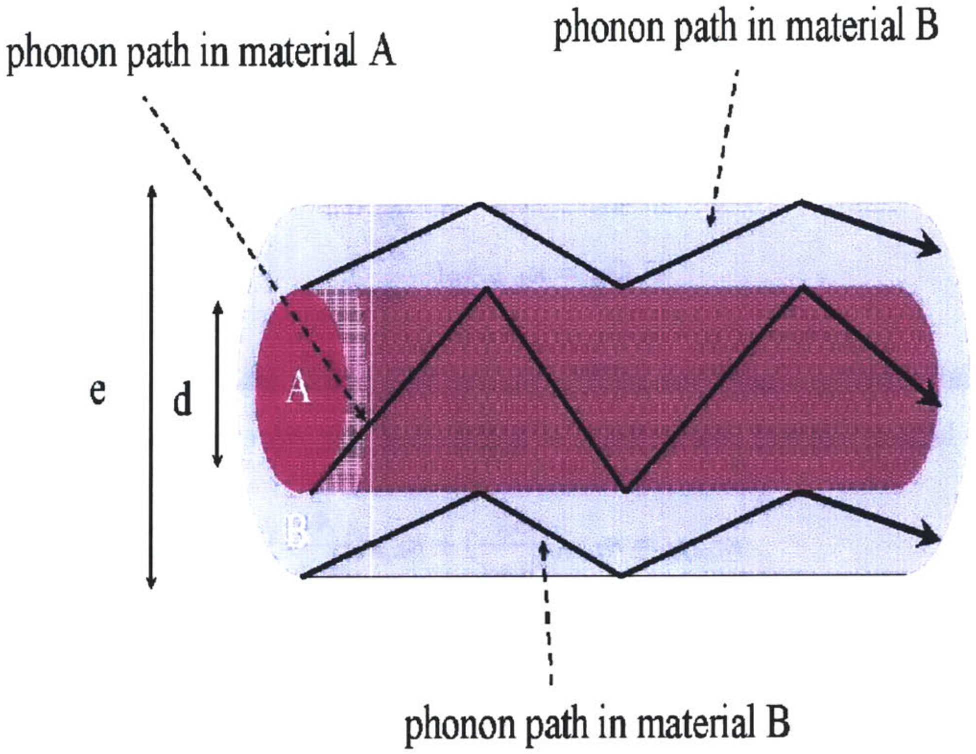

Figure 4-1: A schematic view of the phonon transport in a core-shell nanowire.

where A is the cross sectional area perpendicular to the thermal current direction, T denotes the temperature, and x is the thermal current propagation axis. As a first approximation for the lattice thermal conductivity of a core-shell nanowire, the phonons in each of the two materials are assumed to be independent of one another. Correspondingly, the phonons in each material are assumed to be scattered specularly at the interface. Figure 4-1 summarizes these assumptions.

For a core-shell nanowire with material A as the core and material B as the shell, the total Q_{total} is the sum of Q_A and Q_B,

$$Q_{total} = Q_A + Q_B. \tag{4.19}$$

Using Equation (4.18), each of the terms in Equation (4.19) is given by

$$Q_{total} = \kappa_{L,eff} A_{total}(-\frac{\partial T}{\partial x}), \tag{4.20}$$

$$Q_A = \kappa_{L,A} A_A(-\frac{\partial T}{\partial x}), \tag{4.21}$$

$$Q_B = \kappa_{L,B} A_B(-\frac{\partial T}{\partial x}). \tag{4.22}$$

By substituting Equations (4.20), (4.21), and (4.22) into Equation (4.19), the effective lattice thermal conductivity of a core-shell nanowire is found to be

$$\kappa_{L,eff} = \kappa_{L,A}(\frac{A_A}{A_{total}}) + \kappa_{L,B}(\frac{A_B}{A_{total}}). \tag{4.23}$$

4.3 Thermoelectric Investigations of the Doped Si/SiGe Core-Shell Nanowires

Using the results from Chapter 3 and the formalism developed in Section 4.1 and Section 4.2, modeling of the thermoelectric coefficients for doped Si/SiGe core-shell nanowires is presented in this section. Common n-type dopants for these materials are phosphorus (P) and arsenic (As), while common p-type dopants are boron (B). Results of measurements of the carrier mobility, the lattice thermal conductivity, the heat capacity, and the velocity of sound of Si, Ge, and SiGe alloys are used for the model calculations.

As discussed in Section 3.1, the mobility tensor for Si, Ge, and SiGe alloys is always isotropic due to the cubic symmetry of each of these materials. Using Figures 3-5 and 3-6, the intrinsic mobility values of Si, Ge, and selected compositions of SiGe alloys at room temperature (T=300 K) are extracted and listed in Table 4.1.

Due to the cubic symmetry properties of these materials, the lattice thermal conductivities of Si, Ge, and SiGe alloys are also isotropic. Figure 4-2 shows the thermal resistivity of SiGe alloys as a function of Si concentration x [4]. The thermal con-

Table 4.1: The intrinsic mobility values of Si, Ge, and selected compositions of SiGe alloys at T=300 K. These values are given in $cm^2/(V \cdot s)$.

Ge concentration x	Material	$\mu_e(cm^2/(V \cdot s))$	$\mu_h(cm^2/(V \cdot s))$
0	Si	1400	450
0.05	$Si_{0.95}Ge_{0.05}$	1000	433
0.1	$Si_{0.9}Ge_{0.1}$	800	400
0.2	$Si_{0.8}Ge_{0.2}$	500	267
0.25	$Si_{0.75}Ge_{0.25}$	333	200
0.3	$Si_{0.7}Ge_{0.3}$	267	167
0.4	$Si_{0.6}Ge_{0.4}$	200	120
0.5	$Si_{0.5}Ge_{0.5}$	167	100
0.6	$Si_{0.4}Ge_{0.6}$	200	133
0.7	$Si_{0.3}Ge_{0.7}$	233	167
0.8	$Si_{0.2}Ge_{0.8}$	400	433
0.9	$Si_{0.1}Ge_{0.9}$	1000	733
1	Ge	3900	1900

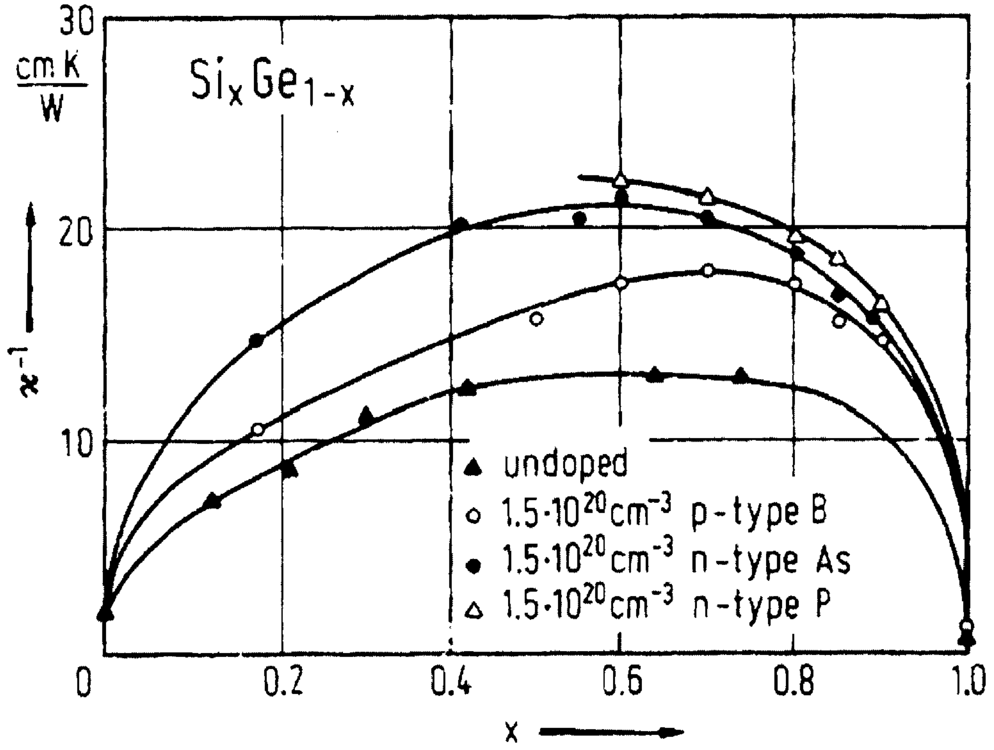

Figure 4-2: Thermal resistivity of SiGe alloys as a function of Si concentration x [4].

Table 4.2: The intrinsic thermal resistivity and thermal conductivity values of Si, Ge, and selected compositions of SiGe alloys at T=300 K.

Ge concentration x	Material	$\kappa_L^{-1}((cm \cdot K)/W)$	$\kappa_L(W/(cm \cdot K))$
0	Si	0.704	1.42
0.05	$Si_{0.95}Ge_{0.05}$	8.07	0.124
0.2	$Si_{0.8}Ge_{0.2}$	12.456	0.0803
0.25	$Si_{0.75}Ge_{0.25}$	12.81	0.0781
0.5	$Si_{0.5}Ge_{0.5}$	12.98	0.077
0.6	$Si_{0.4}Ge_{0.6}$	12.28	0.0814
0.7	$Si_{0.3}Ge_{0.7}$	10.70	0.0934
0.8	$Si_{0.2}Ge_{0.8}$	8.947	0.112
0.9	$Si_{0.1}Ge_{0.9}$	6.49	0.154
1	Ge	1.724	0.58

ductivity of a cubic material is simply the reciprocal of its thermal resistivity. The thermal resistivity and thermal conductivity of Si, Ge, and selected compositions of SiGe alloys at room temperature (T=300 K) are extracted and listed in Table 4.2. Similar to the carrier mobility (see Figure 3-5 and Figure 3-6), the SiGe alloys lattice thermal conductivity shows a significant decrease from pure Si or pure Ge due to the alloying effect. Figure 4-2 also shows the fact that dopants (impurities) decrease the lattice thermal conductivity as well. The heavier the dopant concentration, the more effective it is to decrease the lattice thermal conductivity [23]. But for a good thermoelectric material, it is important that the thermal conductivity decreases much more than the electrical conductivity so that σ/κ increases.

As discussed in Section 4.2, the phonon mean free path of Si, Ge, and SiGe alloys are estimated by the heat capacity (C_v), the velocity of sound for the longitudinal acoustic branch (v_L), the sound velocity for the transverse branches (v_T), and the thermal conductivity (κ_L) (see Equation (4.14) and Equation (4.16)). Table 4.3 lists the values of the C_v, the v_L and the v_T for phonon propagation along [001], the heat capacity, the mass density, and the molar mass of Si and Ge at T=300 K. These values as a function of Ge concentration x for the $Si_{1-x}Ge_x$ alloys at T=300 K are

Table 4.3: Values of sound velocities, heat capacity, and density of Si and Ge at T=300 K.

Material	C_v $(J/(mol \cdot K))$	v_L along [001] $(10^5 cm/s)$	v_T along [001] $(10^5 cm/s)$	density (g/cm^3)	molar mass (g/mol)
Si	19.6	8.43	5.84	2.329	28.09
Ge	22.5	4.91	3.54	5.323	72.64

approximately given by the following expressions [3],

$$C_v = 19.6 + 2.9x\,[J/(mol \cdot K)], \tag{4.24}$$

$$v_{L,[001]} = 8.43 - 3.5162x\,[10^5 cm/s], \tag{4.25}$$

$$v_{T,[001]} = 5.84 - 2.2976x\,[10^5 cm/s], \tag{4.26}$$

$$density = 2.329 + 3.493x - 0.499x^2\,[g/cm^3], \tag{4.27}$$

$$molar\, mass = 28.0855 + 44.5545x\,[g/mol]. \tag{4.28}$$

From Equation (4.24)–(4.28), values of the C_v, the v_L and the v_T for phonon propagation along [001], the mass density, and the molar mass for selected SiGe alloys are estimated. These values are listed in Table 4.4 for reference.

Using values from Table 4.2 to Table 4.4, along with Equation (4.14) and Equation (4.16), the phonon mean free path for bulk Si, Ge, and selected SiGe alloys at T=300 K are calculated and the results are listed in Table 4.5. Applying Equation (4.14), Equation (4.16), Equation (4.17), and Equation (4.23) with the values obtained from Table 4.5, $\kappa_{L,eff}$ could then be found, given constant values of d and e. Table 4.6 and Table 4.7 list the values of $\kappa_{L,eff}$ for selected cases of interest for the core-shell nanowire system at T=300 K. These cases are further studied throughout this chapter.

With all the values needed for the calculation of the transport coefficients for the core-shell nanowire system in place, it is now only a matter of computation to obtain

Table 4.4: Values of sound velocities, heat capacity, and density of selected compositions of SiGe alloys at T=300 K.

x	Material	C_v $(J/(mol \cdot K))$	v_L along [001] $(10^5 cm/s)$	v_T along [001] $(10^5 cm/s)$	density (g/cm^3)	molar mass (g/mol)
0.05	$Si_{0.95}Ge_{0.05}$	19.75	8.254	5.725	2.502	30.313
0.2	$Si_{0.8}Ge_{0.2}$	20.18	7.727	5.380	3.008	36.996
0.25	$Si_{0.75}Ge_{0.25}$	20.33	7.551	5.266	3.171	39.224
0.5	$Si_{0.5}Ge_{0.5}$	21.05	6.672	4.691	3.951	50.363
0.6	$Si_{0.4}Ge_{0.6}$	21.34	6.320	4.461	4.245	54.818
0.7	$Si_{0.3}Ge_{0.7}$	21.63	5.969	4.232	4.530	59.274
0.8	$Si_{0.2}Ge_{0.8}$	21.92	5.617	4.002	4.804	63.729
0.9	$Si_{0.1}Ge_{0.9}$	22.21	5.265	3.772	5.069	68.185

Table 4.5: The calculated values of the phonon mean free path $l_{p,bulk}$ of bulk Si, Ge, and selected compositions of SiGe alloys at T=300 K.

Ge concentration x	Material	$l_{p,bulk}(nm)$
0	Si	85.58
0.05	$Si_{0.95}Ge_{0.05}$	7.62
0.2	$Si_{0.8}Ge_{0.2}$	5.22
0.25	$Si_{0.75}Ge_{0.25}$	5.18
0.5	$Si_{0.5}Ge_{0.5}$	5.72
0.6	$Si_{0.4}Ge_{0.6}$	6.35
0.7	$Si_{0.3}Ge_{0.7}$	7.69
0.8	$Si_{0.2}Ge_{0.8}$	9.76
0.9	$Si_{0.1}Ge_{0.9}$	14.26
1	Ge	57.27

Table 4.6: The calculated values of $\kappa_{L,eff}$ for selected cases of core-shell nanowires at T=300 K.

Case	Material	$d(nm)$	$e(nm)$	$\kappa_{L,eff}(W/(cm \cdot K))$
1	$Si_{0.3}Ge_{0.7}$	3	10	0.0309
2	$Si_{0.3}Ge_{0.7}$	8	10	0.0816
3	$Si_{0.3}Ge_{0.7}$	5	50	0.0697
4	$Si_{0.3}Ge_{0.7}$	45	50	0.401
5	$Si_{0.3}Ge_{0.7}$	28	30	0.306
6	$Si_{0.3}Ge_{0.7}$	3	30	0.0594
7	$Si_{0.1}Ge_{0.9}$	3	10	0.0319
8	$Si_{0.1}Ge_{0.9}$	8	10	0.0813
9	$Si_{0.1}Ge_{0.9}$	5	50	0.0941
10	$Si_{0.1}Ge_{0.9}$	45	50	0.401
11	$Si_{0.1}Ge_{0.9}$	28	30	0.306
12	$Si_{0.1}Ge_{0.9}$	3	30	0.0746
13	$Si_{0.4}Ge_{0.6}$	3	10	0.0306
14	$Si_{0.4}Ge_{0.6}$	8	10	0.0817
15	$Si_{0.4}Ge_{0.6}$	5	50	0.0636
16	$Si_{0.4}Ge_{0.6}$	45	50	0.401
17	$Si_{0.4}Ge_{0.6}$	28	30	0.306
18	$Si_{0.4}Ge_{0.6}$	3	30	0.0553
19	$Si_{0.8}Ge_{0.2}$	3	10	0.0336
20	$Si_{0.8}Ge_{0.2}$	8	10	0.0823
21	$Si_{0.8}Ge_{0.2}$	5	50	0.0653
22	$Si_{0.8}Ge_{0.2}$	45	50	0.401
23	$Si_{0.8}Ge_{0.2}$	28	30	0.307
24	$Si_{0.8}Ge_{0.2}$	3	30	0.0578
25	$Si_{0.75}Ge_{0.25}$	3	10	0.0330
26	$Si_{0.75}Ge_{0.25}$	8	10	0.0822
27	$Si_{0.75}Ge_{0.25}$	5	50	0.0636
28	$Si_{0.75}Ge_{0.25}$	45	50	0.401
29	$Si_{0.75}Ge_{0.25}$	28	30	0.307
30	$Si_{0.75}Ge_{0.25}$	3	30	0.0563
31	$Si_{0.5}Ge_{0.5}$	3	10	0.0310
32	$Si_{0.5}Ge_{0.5}$	8	10	0.0818
33	$Si_{0.5}Ge_{0.5}$	5	50	0.0616
34	$Si_{0.5}Ge_{0.5}$	45	50	0.401
35	$Si_{0.5}Ge_{0.5}$	28	30	0.307
36	$Si_{0.5}Ge_{0.5}$	3	30	0.0541

Table 4.7: The calculated values of $\kappa_{L,eff}$ for selected cases of core-shell nanowires at T=300 K.

Case	Material	$d(nm)$	$e(nm)$	$\kappa_{L,eff}(W/(cm \cdot K))$
37	$Si_{0.95}Ge_{0.05}$	3	10	0.0398
38	$Si_{0.95}Ge_{0.05}$	8	10	0.0829
39	$Si_{0.95}Ge_{0.05}$	5	50	0.0923
40	$Si_{0.95}Ge_{0.05}$	45	50	0.402
41	$Si_{0.95}Ge_{0.05}$	28	30	0.307
42	$Si_{0.95}Ge_{0.05}$	3	30	0.0788
43	$Si_{0.3}Ge_{0.7}$	3	10	0.0309
44	$Si_{0.3}Ge_{0.7}$	8	10	0.0816
45	$Si_{0.3}Ge_{0.7}$	5	50	0.0697
46	$Si_{0.3}Ge_{0.7}$	45	50	0.401
47	$Si_{0.3}Ge_{0.7}$	28	30	0.306
48	$Si_{0.3}Ge_{0.7}$	3	30	0.0594

these transport coefficients. Different cases of the doping concentration, the interface offset (V_{cond} and V_{val}), the total core-shell diameter (e), and the core-shell diameter (d) for both n-type and p-type Si/SiGe core-shell nanowires have been considered. For the n-type Si/SiGe core-shell nanowires, cases where the conduction band offset is $V_{cond} > 0$ and is $V_{cond} < 0$ are both presented, while for the valence band offset, where we only have $V_{val} < 0$, the cases of p-type Si/SiGe core-shell nanowires are investigated. Within each of these cases, various limits of the thermal energy relative to the offset energies are considered, such as the cases where the magnitude of the interface offset $> k_BT$ ($k_BT \approx 26$ meV at T=300 K), $\approx k_BT$, and $< k_BT$. Lastly, the effect of varying the total core-shell diameter (e), and of varying the core diameter (d) are further examined for each of the cases. Figure 4-3 to Figure 4-10 show the calculated ZT as a function of the carrier doping concentration for the core-shell nanowire system for each of these cases at T=300 K. A detailed analysis of the effects of different parameters (doping concentration, V_{cond}, V_{val}, e, and d) are presented in Section 4.4.

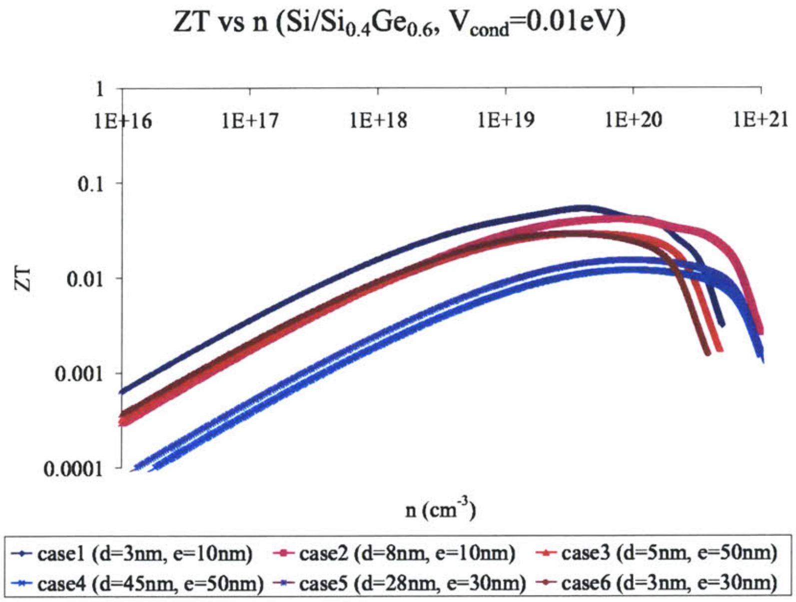

Figure 4-3: Plot of the dimensionless thermoelectric figure of merit ZT versus doping concentration for a n-type Si/SiGe core-shell nanowire with a small positive V_{cond} at T=300 K.

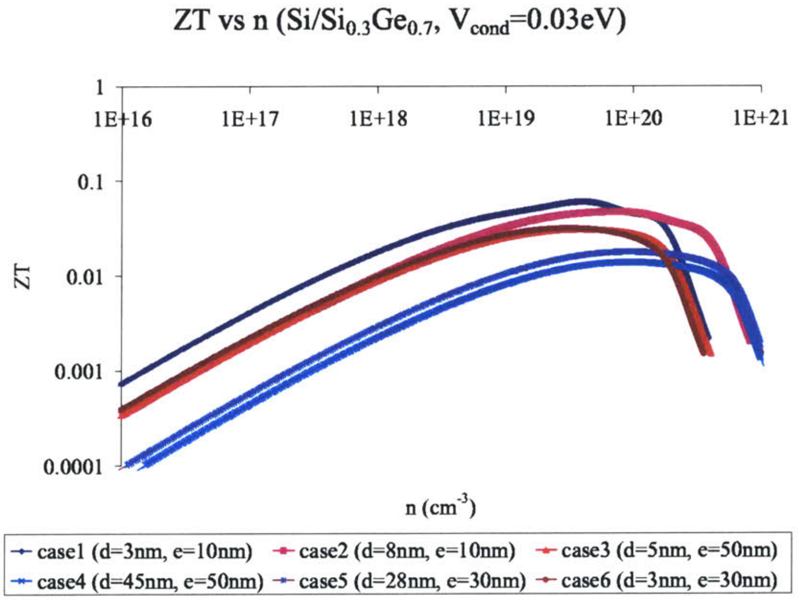

Figure 4-4: Plot of the dimensionless thermoelectric figure of merit ZT versus doping concentration for a n-type Si/SiGe core-shell nanowire with a medium size positive V_{cond} at T=300 K.

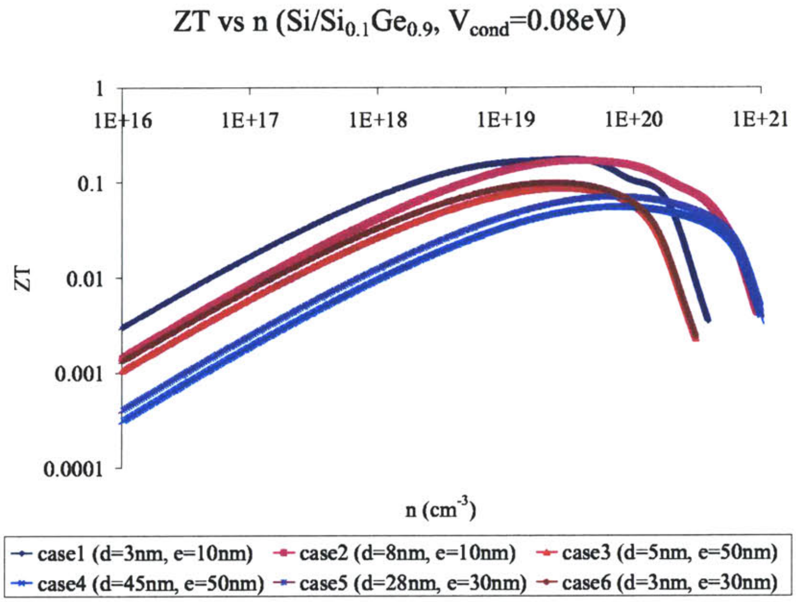

Figure 4-5: Plot of the dimensionless thermoelectric figure of merit ZT versus doping concentration for a n-type Si/SiGe core-shell nanowire with a large positive V_{cond} at T=300 K.

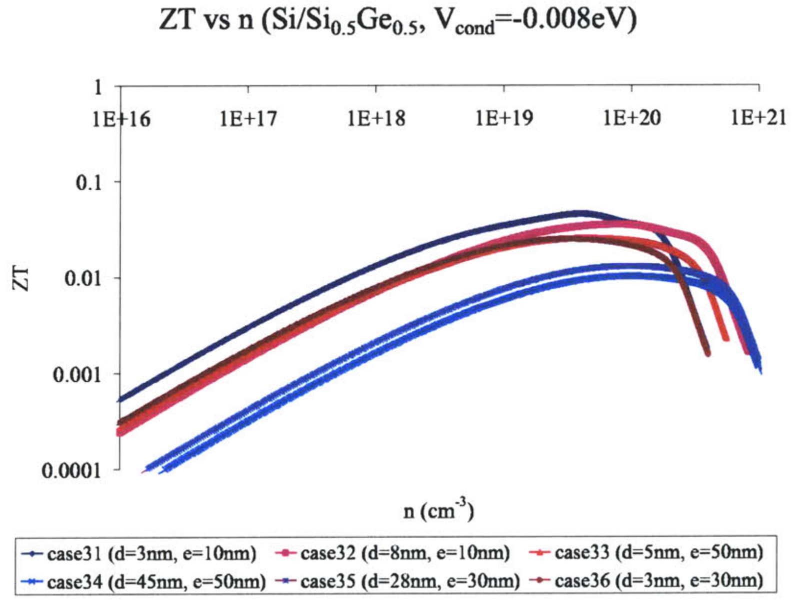

Figure 4-6: Plot of the dimensionless thermoelectric figure of merit ZT versus doping concentration for a n-type Si/SiGe core-shell nanowire with a small negative V_{cond} at T=300 K.

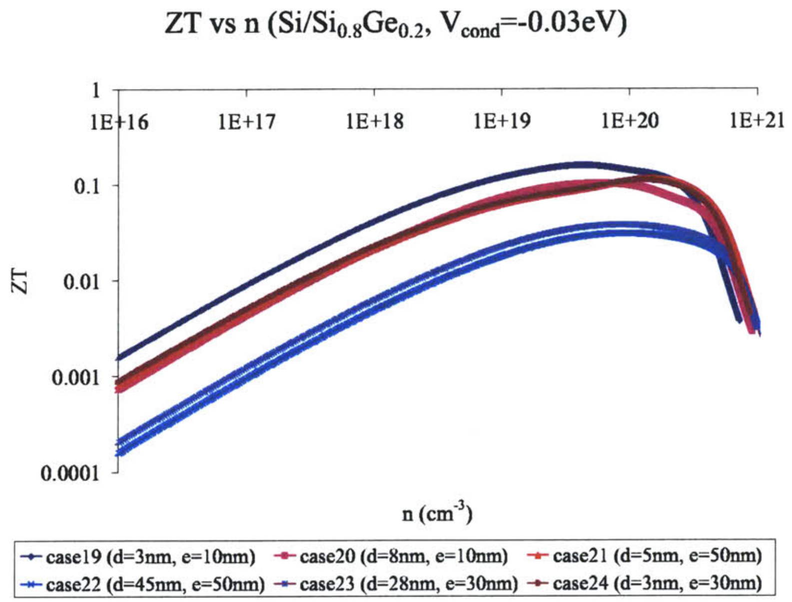

Figure 4-7: Plot of the dimensionless thermoelectric figure of merit ZT versus doping concentration for a n-type Si/SiGe core-shell nanowire with a medium size negative V_{cond} at T=300 K.

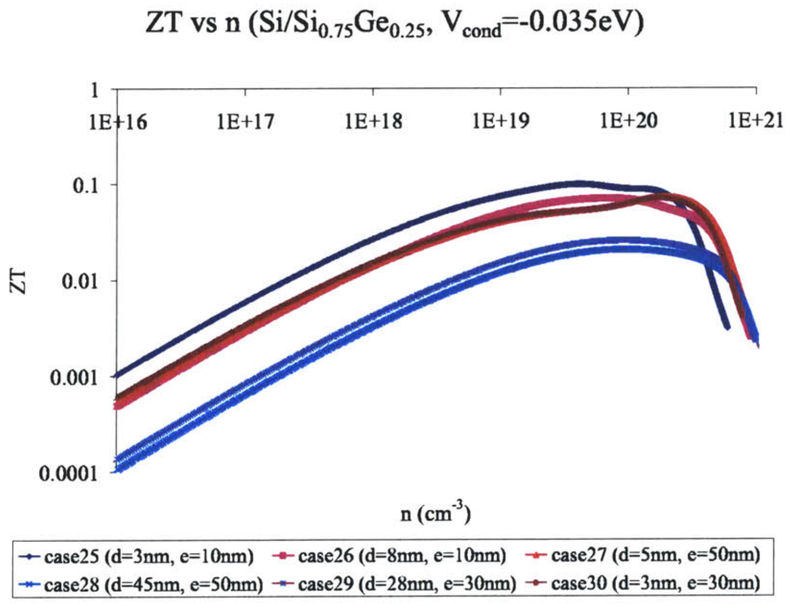

Figure 4-8: Plot of the dimensionless thermoelectric figure of merit ZT versus doping concentration for a n-type Si/SiGe core-shell nanowire with a large negative V_{cond} at T=300 K.

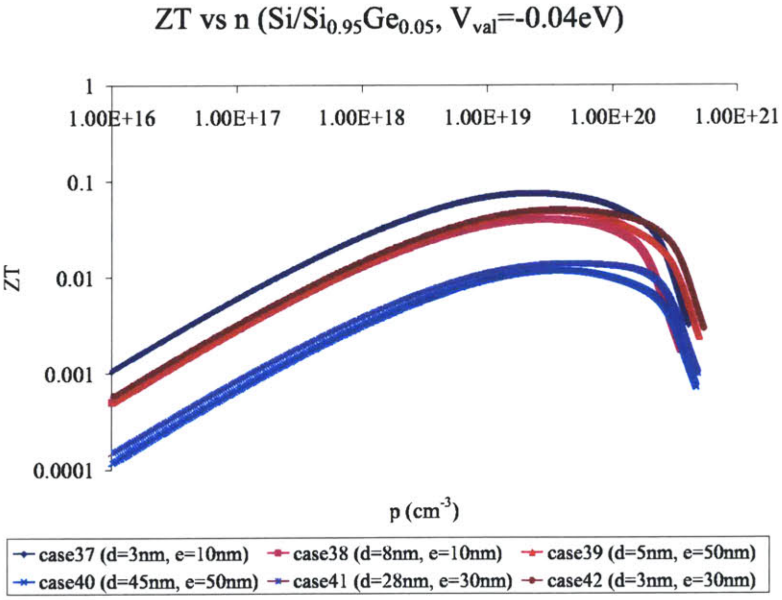

Figure 4-9: Plot of the dimensionless thermoelectric figure of merit ZT versus doping concentration for a p-type Si/SiGe core-shell nanowire with a medium size negative V_{val} at T=300 K.

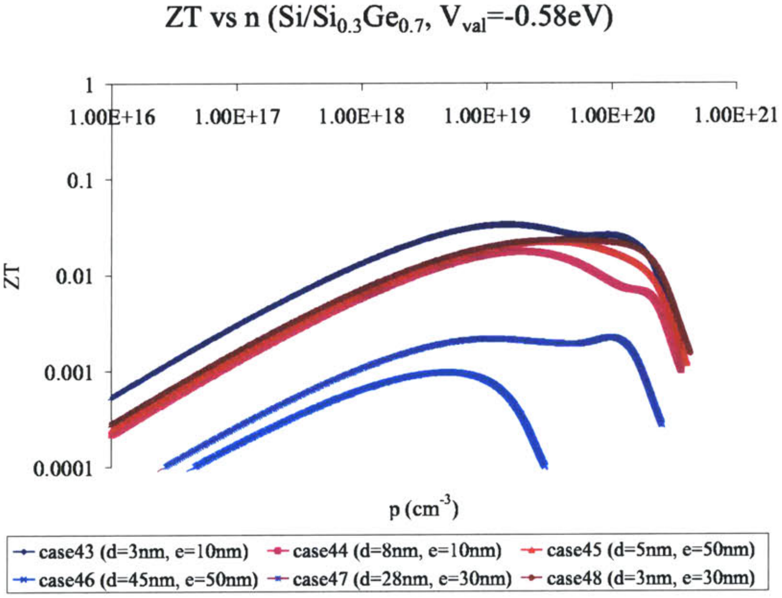

Figure 4-10: Plot of the dimensionless thermoelectric figure of merit ZT versus doping concentration for a p-type Si/SiGe core-shell nanowire with a large negative V_{val} at T=300 K.

4.4 Effect of the different parameters on ZT at T=300 K

As seen from Figure 4-3 to Figure 4-10, the value of ZT changes by a couple orders of magnitude as the carrier doping concentration changes. For each of the cases considered, there occurs an optimal value of carrier doping concentration. The value of both the optimal carrier doping concentration and its corresponding ZT are different from one another. Table 4.8 and Table 4.9 list the values of the optimal doping concentration (n_{opt} or p_{opt}) along with its corresponding values of σ, S, κ_e, and ZT for each case. The effect of carrier doping concentration on ZT is discussed in Section 4.4.1. The effect of the interface offset, the total core-shell diameter (e), and the core diameter (d) that leads to the difference in the values of ZT and its corresponding optimal doping concentration is reviewed in Section 4.4.2, Section 4.4.3, and Section 4.4.4, respectively.

4.4.1 Effect of the Doping Concentration

The carrier doping concentration plays a major role in the determination of the value of ZT as seen from Figure 4-3 to Figure 4-10. The carrier doping concentration has a one-to-one dependence on the Fermi level of the system. Consider an n-type semiconductor material as an example. As an illustration, assume the thermal conductivity is dominated by phonons, which is usually true for a semiconductor. As the Fermi level E_f moves from the edge of the valence band to the edge of the conduction band, the concentration of the electrons in the conduction band increases. The transport coefficient S and σ both depend on the concentration of the electrons. When E_f is near the edge of the valence band, the concentration of carriers (electrons) is low, resulting in a low σ and a large S. As the Fermi level E_f increases toward the conduction band edge, the concentration of the electrons increases, leading to a smaller S and a larger σ. Since decreasing the rate of S and increasing the rate of σ are different,

Table 4.8: The values of n_{opt}, σ, S, κ_e and ZT for different cases at T=300 K.

Case	V_{cond} (eV)	n_{opt} $(10^{19}cm^{-3})$	σ $(10^4 S/m)$	S $(10^{-4}V/K)$	κ_e $(W/(m \cdot K))$	ZT
1	0.03	4.039	4.990	-1.170	0.326	0.060
2	0.03	7.350	9.081	-1.225	0.587	0.047
3	0.03	3.863	4.773	-1.248	0.308	0.031
4	0.03	9.422	11.64	-1.271	0.737	0.014
5	0.03	9.273	11.46	-1.274	0.727	0.018
6	0.03	3.135	3.873	-1.295	0.246	0.031
7	0.08	3.131	16.61	-1.238	1.138	0.176
8	0.08	3.737	19.82	-1.629	1.239	0.168
9	0.08	2.760	14.64	-1.428	0.909	0.087
10	0.08	7.599	40.30	-1.396	2.522	0.055
11	0.08	7.218	38.28	-1.428	2.396	0.071
12	0.08	2.379	12.62	-1.470	0.779	0.099
13	0.01	4.023	4.267	-1.184	0.279	0.054
14	0.01	7.696	8.162	-1.209	0.530	0.041
15	0.01	4.128	4.378	-1.214	0.286	0.029
16	0.01	9.593	10.17	-1.267	0.645	0.012
17	0.01	9.480	10.05	-1.263	0.639	0.015
18	0.01	3.233	3.428	-1.275	0.219	0.029
19	-0.03	4.345	11.52	-1.388	0.785	0.161
20	-0.03	5.919	15.69	-1.420	0.999	0.103
21	-0.03	14.871	39.43	-0.957	2.816	0.116
22	-0.03	9.295	24.64	-1.322	1.554	0.031
23	-0.03	8.575	22.74	-1.343	1.433	0.038
24	-0.03	12.996	34.46	-0.951	2.479	0.113
25	-0.035	4.143	7.315	-1.312	0.491	0.100
26	-0.035	6.825	12.05	-1.324	0.773	0.071
27	-0.035	19.502	34.44	-0.792	2.465	0.073
28	-0.035	9.668	17.07	-1.292	1.079	0.021
29	-0.035	9.188	16.23	-1.297	1.027	0.026
30	-0.035	18.124	32.00	-0.768	2.297	0.071
31	-0.008	4.024	3.563	-1.193	0.231	0.046
32	-0.008	7.802	6.910	-1.211	0.445	0.035
33	-0.008	4.362	3.863	-1.183	0.254	0.025
34	-0.008	9.895	8.762	-1.255	0.555	0.010
35	-0.008	9.697	8.588	-1.253	0.546	0.013
36	-0.008	3.257	2.885	-1.269	0.184	0.025

Table 4.9: The values of p_{opt}, σ, S, κ_e and ZT for different cases at T=300 K.

Case	V_{val} (eV)	p_{opt} $(10^{19}cm^{-3})$	σ $(10^4 S/m)$	S $(10^{-4}V/K)$	κ_e $(W/(m \cdot K))$	ZT
37	-0.04	2.253	5.174	1.441	0.325	0.075
38	-0.04	2.752	6.318	1.346	0.398	0.040
39	-0.04	3.460	7.945	1.408	0.486	0.049
40	-0.04	3.625	8.323	1.380	0.504	0.012
41	-0.04	4.590	10.54	1.174	0.687	0.014
42	-0.04	3.674	8.435	1.294	0.547	0.050
43	-0.58	1.462	1.295	1.651	0.071	0.033
44	-0.58	1.895	1.678	1.682	0.085	0.017
45	-0.58	3.234	2.864	1.355	0.175	0.022
46	-0.58	0.479	0.424	1.741	0.019	0.001
47	-0.58	9.730	8.616	0.517	0.610	0.002
48	-0.58	3.900	3.454	1.170	0.228	0.023

a maximum value of ZT results at some intermediate Fermi level. Therefore, there always exists an optimal concentration (n_{opt} or p_{opt}) for each of the cases considered (see Figure 4-3 to Figure 4-10).

The values of optimal concentration (n_{opt} or p_{opt}) and its corresponding ZT for the cases considered are listed in Table 4.8 and Table 4.9. One should note that both n_{opt} and p_{opt} are in the order of $10^{19}cm^{-3}$. The effect that leads to the difference in the value of the optimal ZT and the optimal concentration (n_{opt} or p_{opt}) for these cases will be discussed in the following subsections.

4.4.2 Effect of the Interface Offset

There are three different types of interface offsets involved in the core-shell nanowire system: V_{cond} >0, V_{cond} <0, and V_{val} <0. These cases will each be examined individually in this subsection.

For the case of V_{cond} >0, the Si core region acts like a potential well. From Figure 4-3 to Figure 4-5, one sees that as V_{cond} increases, the ZT increases. This suggests that a system with some confinement is better than a system without any confinement. However, with a more careful examination, this effect may also be due to the choice of selection in the examples. The cases considered here also show an increase in mobility as V_{cond} increases due to the change in the shell composition away from the $Si_{0.5}Ge_{0.5}$ composition (see Figure 3-5). This increase in mobility could be the dominant factor for the increase in the value of ZT.

For the case of $V_{cond} < 0$, as its magnitude increases, ZT first increases, then decreases. This result is not consistent with the result from the $V_{cond} > 0$ case. However, this finding is consistent with the previous conclusion when viewed using the changes in alloy compositions. From Figure 4-6 to Figure 4-8, it is clear that as the composition of the shell layer gets further away from the $Si_{0.5}Ge_{0.5}$ composition, the value of ZT increases. As mentioned before, this increase in ZT is due to the increase in mobility of the system. Thus, these findings suggest that the effect of the conduction band offset on ZT is not as significant as the electron mobility. One possible cause for that is connected with the small magnitude of the conduction band offset.

Lastly, for the case of $V_{val} < 0$, as its magnitude increases, ZT decreases dramatically. This large drop in the value of ZT is mainly due to the large confinement effect. Similar to the last two cases, the results could be better interpreted in terms of mobility. Once again, it is observed that the value of ZT decreases as the carrier (hole) mobility decreases. These findings suggest that a large band offset is not good from a thermoelectric point of view for the core-shell nanowire system in which conduction is expected through both the core and the shell regions.

The results above suggest that for the core-shell nanowire system with which conduction is expected through both regions, a small offset in either the conduction band or the valence band will have very little effect on the system's thermoelectric performance, while a large interface band offset will greatly degrade its thermoelectric performance. On the other hand, the carrier mobility has a major effect on the determination of the system's thermoelectric performance. These conclusions suggest that a good core-shell nanowire system candidate is the one with a shell composition that results in both a high mobility in the shell and a small interface band offset for the carriers.

4.4.3 Effect of the Total Core-Shell Diameter (e)

For all the different cases considered, a similar behavior for the value of the optimal concentration and its corresponding ZT with respect to the total core-shell diameter (e) is observed. As seen from Figure 4-3 to Figure 4-10, as e increases, the optimal carrier concentration increases and its corresponding ZT decreases. The e effect is most dominant in the case of V_{val} <0 and is large in magnitude. It seems that this effect is especially dominant when the magnitude of the confinement (V_{cond} or V_{val}) is large ($>> k_BT \approx 26\,\mathrm{meV}$ at T=300 K). At the same time, it is observed that the optimal concentration and its corresponding value of ZT also depend on d. The effect of d will be considered in the next section.

The observations found in this section suggest that a good core-shell nanowire system candidate for thermoelectric applications is one with a small e. For the cases considered, a value of 10 nm to 20 nm for e is a desired choice.

4.4.4 Effect of the Core Diameter (d) and the Shell Thickness (($e-d)/2$)

When compared with the effect of e on ZT, a similar behavior is observed for the effect of d on the core-shell nanowire system. From Figure 4-3 to Figure 4-10, it is observed that as d increases, the optimal carrier doping concentration increases, whereas its corresponding ZT decreases for all the cases. A rather unusual behavior is seen in the case of large e and V_{val} <0 with a large magnitude. For this specific case, the optimal carrier concentration actually decreases as d increases, and its corresponding value of ZT decreases dramatically compared to the other cases. This strange behavior could be due to the large hole confinement effect.

4.4.5 Conclusions

From these subsections, one sees that in order for the core-shell nanowire system to have good thermoelectric performance, it should be an n-type material, have a small *e* and a small *d*, and have a relatively high mobility shell composition.

Similar to the previous results for bulk materials [24], the n-type core-shell nanowire shows a better thermoelectric performance than its p-type counterpart. This finding is mainly due to the difference in the mobility of the two materials.

As for the geometric factors of *e* and *d*, the small value of *e* gives enhancement in the thermoelectric performance due to the increase in quantum mechanical confinement effect, whereas the small value of *d* is desired for minimizing the contribution of the large value of the Si lattice thermal conductivity. The examples that were selected suggest that an *e* of 10nm and a *d* of 3nm result in good thermoelectric performance. On the other hand, the effect of the conduction band offset or the valence band offset is not as dominant as is the mobility, as mentioned before.

It is concluded that a good thermoelectric performance core-shell nanowire system should have a shell that is relatively high in mobility (a shell composition that is close to pure Si or pure Ge), a small total core-shell diameter, and a small core diameter. The system should also be an n-type system. Thus, it would be ideal to have systems similar to the systems of case 7 or case 19.

4.5 Comparison between the Core-Shell Nanowire and the Nanowire

A similar calculation is applied to selected cases of the Si and $Si_{0.3}Ge_{0.7}$ nanowire system at T=300 K for comparison. The nanowire is further studied for both the n-type and p-type cases using two different diameters of 10nm and 50nm. Figure 4-11

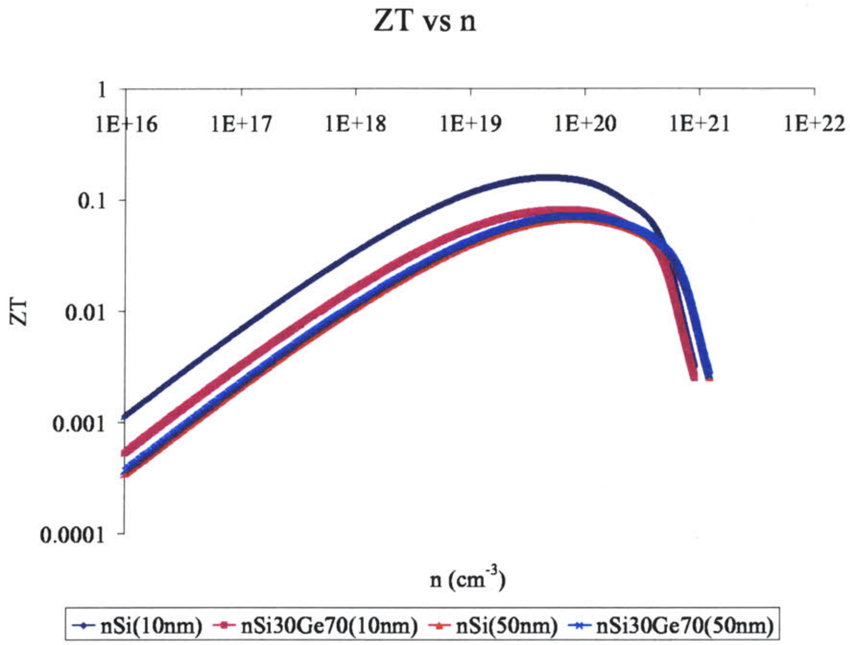

Figure 4-11: Plot of the dimensionless thermoelectric figure of merit ZT versus doping concentration for a n-type nanowire at T=300 K.

and Figure 4-12 show the calculated ZT for these cases as a function of the carrier doping concentration. The values of interest in these cases are summarized in Table 4.10.

Comparing the results from Table 4.10 with Table 4.8 and Table 4.9 for the Si nanowire cases, the core-shell nanowire system shows a very promising result. For example, the 10nm n-type Si nanowire system has a ZT value of 0.1583 at the optimal electron concentration of $4.892 \times 10^{19} cm^{-3}$. However, the 10nm n-type Si/SiGe core-shell nanowire system with a 3nm core diameter can have a ZT value of up to 0.1763 given a conduction band offset of 0.08 eV. This comparison reinforces previous conclusions about the improvement in thermoelectric performance with a core-shell nanowire system.

On the other hand, comparison between the Si/SiGe core-shell nanowire system and the SiGe nanowire system shows that SiGe nanowire system has a better perfor-

Table 4.10: The values of optimal concentration, σ, S, κ_e, $\kappa_{L,eff}$, and ZT for different cases of nanowire system at T=300 K.

Case	Material	e (nm)	Optimal Concentration ($10^{19} cm^{-3}$)	σ ($10^4 S/m$)	S ($10^{-4} V/K$)	κ_e ($W/(m \cdot K)$)	$\kappa_{L,eff}$ ($W/(cm \cdot K)$)	ZT
101	n-Si	10	4.892	36.32	-1.578	2.271	0.149	0.158
102	n-Si	50	8.242	61.19	-1.429	3.796	0.524	0.067
103	p-Si	10	3.028	7.226	1.258	0.462	0.149	0.022
104	p-Si	50	3.976	9.487	1.322	0.582	0.524	0.009
105	n-$Si_{0.3}Ge_{0.7}$	10	6.614	8.173	-1.381	0.519	0.053	0.081
106	n-$Si_{0.3}Ge_{0.7}$	50	8.081	9.984	-1.442	0.619	0.081	0.072
107	p-$Si_{0.3}Ge_{0.7}$	10	3.028	2.682	1.258	0.172	0.053	0.023
108	p-$Si_{0.3}Ge_{0.7}$	50	3.760	3.330	1.358	0.204	0.081	0.022

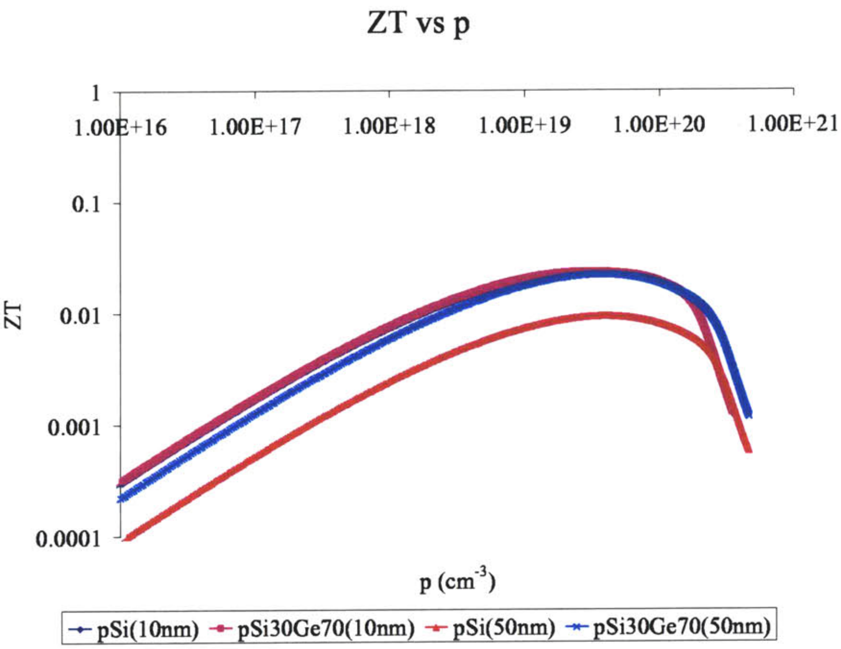

Figure 4-12: Plot of the dimensionless thermoelectric figure of merit ZT versus doping concentration for a p-type nanowire at T=300 K.

mance. This conclusion is somewhat misleading due to the conservative assumptions for the model used in this thesis. In this model, the value of the carrier mobility of the SiGe-strained layer is taken to be the same as the bulk SiGe alloys carrier mobility. However, many previous calculations have shown that the carrier mobility in the strained SiGe layer is much higher than the carrier mobility of the bulk SiGe. For example, the hole mobility of a strained $Si_{0.8}Ge_{0.2}$ layer on a Si substrate is calculated to be at least $900\,cm^2/(V \cdot s)$ [25], whereas the hole mobility of a bulk $Si_{0.8}Ge_{0.2}$ alloy is about $267\,cm^2/(V \cdot s)$. Thus, with the mobility issue relaxed, we would expect that the core-shell nanowire system would have a better thermoelectric performance than its bulk and nanowire counterparts.

Chapter 5

Conclusions and Future Directions

This thesis concludes with the findings and some thoughts for future research studies. These are summarized in the following sections.

5.1 Conclusions

In this thesis, a model for the core-shell nanowire system is developed and presented. The thermoelectric-related transport properties of the Si core SiGe shell core-shell nanowire is extensively studied from a theoretically standpoint.

Using the band structure of the SiGe strained layer on a Si substrate as a guideline, the band structure of the strained SiGe shell layer of a Si core SiGe shell core-shell nanowire is developed. Due to the cylindrical structure of the core-shell nanowire, the degeneracy of the conduction pockets for the strained SiGe shell layer is modeled differently than its 2D SiGe strained epitaxial layer on a Si substrate.

Theoretical investigation of the thermoelectric properties of a Si/SiGe core-shell nanowire suggests that the system with a small interface offset between the core and the shell materials (V), a small total core-shell diameter (e), a small core diameter (d), and a shell with a composition that results in a high mobility are very promising in thermoelectric performance. The main reason for this finding is that a small e and a small interface band offset give rise to a system with better quantum mechanical properties, while a small d minimizes the high thermal conductivity contribution from the Si core. As for the shell composition, it is a rule of thumb that a higher carrier mobility results in an enhancement in the thermoelectric performance. Similar to the previous investigation on bulk materials and nanowires, this thesis' finding also suggests that an n-type material has a much better thermoelectric performance than its p-type counterpart. This result is mainly due to the difference in carrier mobility for the p-type and n-type materials.

The thermoelectric-related transport properties for a Si/SiGe core-shell nanowire are compared with the relating properties for a Si nanowire and a SiGe nanowire. The Si/SiGe core-shell nanowire indeed shows a better thermoelectric performance than its Si nanowire counterpart, largely due to the decreases thermal conductivity of the core-shell structure. However, due to the harsh approximations made to the carrier mobility for the Si/SiGe core-shell nanowire system, its thermoelectric properties are slightly outperformed by its SiGe nanowire counterpart. But with the harsh conditions imposed on the carrier mobility of the Si/SiGe core-shell nanowire structure in this thesis relaxed, there is much confidence that the thermoelectric performance of the Si/SiGe core-shell nanowire structure could be made to be better than its SiGe nanowire counterpart.

5.2 Future Directions

Si/SiGe core-shell nanowire investigated in this thesis is an interesting low dimensional system for research study. This Si/SiGe core-shell nanowire system shows possibilities for a very promising enhancement in thermoelectric performance. From the cases that have been investigated in this thesis, more ideas along the directions that were considered have been stimulated and these ideas are worthy of further exploration.

First, it is very valuable to better understand the band structure of the Si/SiGe core-shell nanowire system. Experiments should be performed to pursue the basic understanding of the band structure of the Si/SiGe nanowire. More experiments should then be carried out to further explore the diameter effect and the strain effect to the band structure of SiGe. With these findings in hand, the compositional grading effect in the interface region should also be investigated and taken into account for extending the present theoretical model.

Secondly, the high temperature regime should be investigated in some detail. Currently, the most common thermoelectric application for a SiGe alloy is energy generation in space in high temperature ranges ($\sim 600\,^{o}$C - $700\,^{o}$C). Thus more theoretical investigation and more experiments should be carried out in the high temperature regime to further understand this Si/SiGe core-shell nanowire system so that better thermoelectric materials could be made for future space applications.

Lastly, the effect of the surrounding of the core-shell nanowire should be taken into consideration for better understanding of the properties of the proposal nanocomposite structure. This is a very crucial and essential step so that this self-assembled nano-materials system could be made competitive and cost-effective. Experiments should be carried out to further understand the thermoelectric implications of the various self-assembly procedures and the difficulties associated with achieving the nanocomposite materials. Finally, nanocomposite materials made from nanoparticles should be studied both experimentally and theoretically.

Bibliography

[1] http://www.ioffe.rssi.ru/SVA/NSM/Semicond/Si.

[2] http://www.ioffe.rssi.ru/SVA/NSM/Semicond/Ge.

[3] M.E. Levinshtein, S.L. Rumyantsev, and M.S. Shur, in *Properties of Advanced Semiconductor Materials: GaN, AlN, InN, BN, SiC, SiGe*, chapter 6, (Wiley, New York, 2001).

[4] K.H. Hellwege, in *Zahlenwerte und Funktionen aus Naturwissenschaften und Technik*, section 1.6, (Springer-Verlag, Berlin, 1961-<c1996>).

[5] E Kasper and K Lyutovich, in *Properties of Silicon Germanium and SiGe: Carbon*, chapter 4, (INSPEC, London, 2000).

[6] H.J. Goldsmid, *Thermoelectric Refrigeration* (Plenum Press, New York, 1964).

[7] L. D. Hicks and M. S. Dresselhaus, Phys. Rev. B **47**, 12727–12731 (1993).

[8] L. D. Hicks and M. S. Dresselhaus, Phys. Rev. B **47**, 16631–16634 (1993).

[9] R. Venkatasubramanian, E. Siivola, T. Colpitts, and B. O'Quinn, Nature **413**, 597–602 (October 2001).

[10] Y.-M. Lin. Fabrication, Characterization, and Theoretical Modeling of the Te-doped Bi nanowire system for thermoelectric applications. Master's thesis, Massachusetts Institute of Technology, Department of Electrical Engineering and Computer Science, 2000.

[11] T.P. Orlando, S.D. Senturia, and P.L. Hagelstein. Physics for Solid State Applications. Chapter 7 of MIT 6.730 Course Notes.

[12] P.L. Hagelstein. Introduction to Numerical Simulation. Chapter 12 of MIT 6.673 Course Notes.

[13] K.H. Hellwege, in *Zahlenwerte und Funktionen aus Naturwissenschaften und Technik*, section 1.2, (Springer-Verlag, Berlin, 1961-<c1996>).

[14] K.H. Hellwege, in *Zahlenwerte und Funktionen aus Naturwissenschaften und Technik*, section 1.3, (Springer-Verlag, Berlin, 1961-<c1996>).

[15] J. W. Matthews, *Epitaxial growth* (Academic Press, New York, 1975).

[16] N.E. Ashcroft and N.D. Mermin, in *Solid State Physics*, chapter 13, (Saunders College Publishing, New York, 1976).

[17] X. Sun, Z. Zhang, and M. S. Dresselhaus, Appl. Phys. Lett. **74**, 4005–4007 (1999).

[18] T. Koga, T. C. Harman, S. B. Cronin, and M. S. Dresselhaus, Phys. Rev. B **60**, 14286–14293 (1999).

[19] C. Dames and G. Chen, J. Appl. Phys. **95**(2), 682–693 (January 2004).

[20] N.E. Ashcroft and N.D. Mermin, in *Solid State Physics*, chapter 25, (Saunders College Publishing, New York, 1976).

[21] T.P. Orlando, S.D. Senturia, and P.L. Hagelstein. Physics for Solid State Applications. Chapter 4 of MIT 6.730 Course Notes.

[22] N.E. Ashcroft and N.D. Mermin, in *Solid State Physics*, chapter 1, (Saunders College Publishing, New York, 1976).

[23] M. S. Dresselhaus and J. P. Heremans. In *Thermoelectrics Handbook: Macro to Nano-Structured Materials*, edited by D. M. Rowe, CRC Press, Inc., Boca Raton, Florida, USA, 2004. Chapter.

[24] T.H. Geballe and G.W. Hull, Phys. Rev. **94**(5), 1134–1140 (June 1954).

[25] S.K. Chun and K.L. Wang, IEEE Transactions on Electron Devices **39**(9), 2153–2164 (September 1992).